

# Electromechanical vortex filaments during cardiac fibrillation

J. Christoph<sup>1,2,3</sup>, M. Chebbok<sup>2,4</sup>, C. Richter<sup>1,2,4</sup>, J. Schröder-Schetelig<sup>1,2,3</sup>, P. Bittihn<sup>5</sup>, S. Stein<sup>1,3</sup>, I. Uzelac<sup>6</sup>, F. H. Fenton<sup>6</sup>, G. Hasenfuß<sup>2,4</sup>, R. F. Gilmour Jr<sup>7</sup> & S. Luther<sup>1,2,3,8,9,10</sup>

**The self-organized dynamics of vortex-like rotating waves, which are also known as scroll waves, are the basis of the formation of complex spatiotemporal patterns in many excitable chemical and biological systems<sup>1–4</sup>. In the heart, filament-like phase singularities<sup>5,6</sup> that are associated with three-dimensional scroll waves<sup>7</sup> are considered to be the organizing centres of life-threatening cardiac arrhythmias<sup>7–13</sup>. The mechanisms that underlie the onset, maintenance and control<sup>14–16</sup> of electromechanical turbulence in the heart are inherently three-dimensional phenomena. However, it has not previously been possible to visualize the three-dimensional spatiotemporal dynamics of scroll waves inside cardiac tissues. Here we show that three-dimensional mechanical scroll waves and filament-like phase singularities can be observed deep inside the contracting heart wall using high-resolution four-dimensional ultrasound-based strain imaging. We found that mechanical phase singularities co-exist with electrical phase singularities during cardiac fibrillation. We investigated the dynamics of electrical and mechanical phase singularities by simultaneously measuring the membrane potential, intracellular calcium concentration and mechanical contractions of the heart. We show that cardiac fibrillation can be characterized using the three-dimensional spatiotemporal dynamics of mechanical phase singularities, which arise inside the fibrillating contracting ventricular wall. We demonstrate that electrical and mechanical phase singularities show complex interactions and we characterize their dynamics in terms of trajectories, topological charge and lifetime. We anticipate that our findings will provide novel perspectives for non-invasive diagnostic imaging and therapeutic applications.**

Spiral waves are found ubiquitously throughout nature<sup>1–4</sup>. These spiral waves form dynamically in many chemical and biological systems around two- or three-dimensional centres of rotation, which consist of singular points or filament-like lines of phase singularity<sup>5,6</sup>, respectively. In the heart, spiral waves are associated with cardiac fibrillation<sup>7,8</sup>, as electrical vortex-like rotating waves or rotors can be observed on the surface of the heart during arrhythmia<sup>9</sup>. The core regions of these rotors, which can be displayed as phase singularities using fluorescence imaging of membrane voltage or calcium<sup>12,13</sup>, are thought to expand into the heart muscle where they form vortex filaments that are associated with three-dimensional (3D) electrical scroll waves<sup>5</sup>. However, visualization of the 3D wave phenomena that occur within the cardiac muscle has remained a major scientific challenge. Despite substantial progress in the development of tomographic optical techniques<sup>17–19</sup>, the measurement of transient electrical scroll waves inside cardiac tissue has so far been impossible. Because vortex filaments are considered to be the organizing centres of fibrillation<sup>12,13</sup>, insights into their dynamics

inside the heart wall are thought to be key to understanding the nature of cardiac fibrillation<sup>10–13</sup> and to the conceptualization and advancement of novel techniques for the control of heart rhythm disorders<sup>14–16</sup>.

Here, we present direct and fully time-resolved measurements of 3D mechanical scroll waves inside the contracting cardiac muscle of intact, Langendorff-perfused pig hearts. To elucidate the dynamics of electrical and mechanical wave phenomena in the heart, we combined panoramic fluorescence imaging (optical mapping) with high-resolution four-dimensional (4D) ultrasound imaging (Fig. 1 and Extended Data Figs 1–3). The rapid mechanical contractions within the entire ventricles during ventricular fibrillation were measured using fast 4D ultrasound imaging with a spatiotemporal resolution of 0.5–1.0 mm (field of view, approximately  $10 \times 10 \times 10 \text{ cm}^3$ ) and 50–188 Hz volumes per second (see Methods). Tissue deformation (strain) was calculated from the 4D ultrasound data, revealing the propagation of 3D mechanical waves of contracting and dilating tissue throughout the ventricular muscle during regular rhythm and cardiac arrhythmias (Fig. 1a, d, 2a). From the amplitude of the mechanical deformation wave, the corresponding phase was computed. We induced ventricular tachycardia and ventricular fibrillation in  $n = 5$  pig hearts (see Methods). During ventricular tachycardia, we observed a single stable 3D mechanical scroll wave within the left-ventricular wall (Supplementary Video 1). The phase of this 3D wave (Fig. 1a, d and Extended Data Fig. 1a, b) revealed the formation a U-shaped vortex filament, which extends from the epicardial surface to deep inside the left ventricular wall and back. On the surface of the heart, the filament ended in two phase singularities with opposite topological charges, corresponding to two stable counter-rotating mechanical spiral waves. During ventricular fibrillation, drifting U-shaped mechanical filaments were observed during ventricular fibrillation (Fig. 2a). In this example, the breakthrough of the filament through the epicardial surface resulted in the formation of two transient I-shaped filaments and two corresponding counter-rotating, outwardly drifting mechanical scroll waves (Supplementary Video 2 and Extended Data Fig. 1c). The formation, transition and extinction of U-shaped, I-shaped and O-shaped mechanical filaments was also observed during ventricular fibrillation (Fig. 2b), phenomena similar to those predicted by models for electrical filaments<sup>5</sup>. The mechanical wave phenomena that were obtained from tissue deformation analyses using ultrasound imaging were compared to the electrical activation and mechanical motion data that were obtained from simultaneous multi-modal optical mapping of the surface of the heart (see Supplementary Video 9 and Extended Data Figs 4d, e, 9). The optical mapping data confirmed the co-existence of rotating waves of mechanical deformation and electrical activation, which appeared simultaneously within the same region of the heart and exhibited the same rotational sense and rotation period, and retained a similar morphological shape

<sup>1</sup>Max Planck Institute for Dynamics and Self-Organization, Göttingen, Germany. <sup>2</sup>German Center for Cardiovascular Research (DZHK), Partner Site Göttingen, Göttingen, Germany. <sup>3</sup>Institute for Nonlinear Dynamics, University of Göttingen, Göttingen, Germany. <sup>4</sup>Department for Cardiology and Pneumology, University Medical Center Göttingen, Göttingen, Germany. <sup>5</sup>BioCircuits Institute, University of California San Diego, La Jolla, California, USA. <sup>6</sup>School of Physics, Georgia Institute of Technology, Atlanta, Georgia, USA. <sup>7</sup>University of Prince Edward Island, Charlottetown, Prince Edward Island, Canada. <sup>8</sup>Institute of Pharmacology, University Medical Center Göttingen, Göttingen, Germany. <sup>9</sup>Department of Bioengineering, Northeastern University, Boston, Massachusetts, USA. <sup>10</sup>Department of Physics, Northeastern University, Boston, Massachusetts, USA.

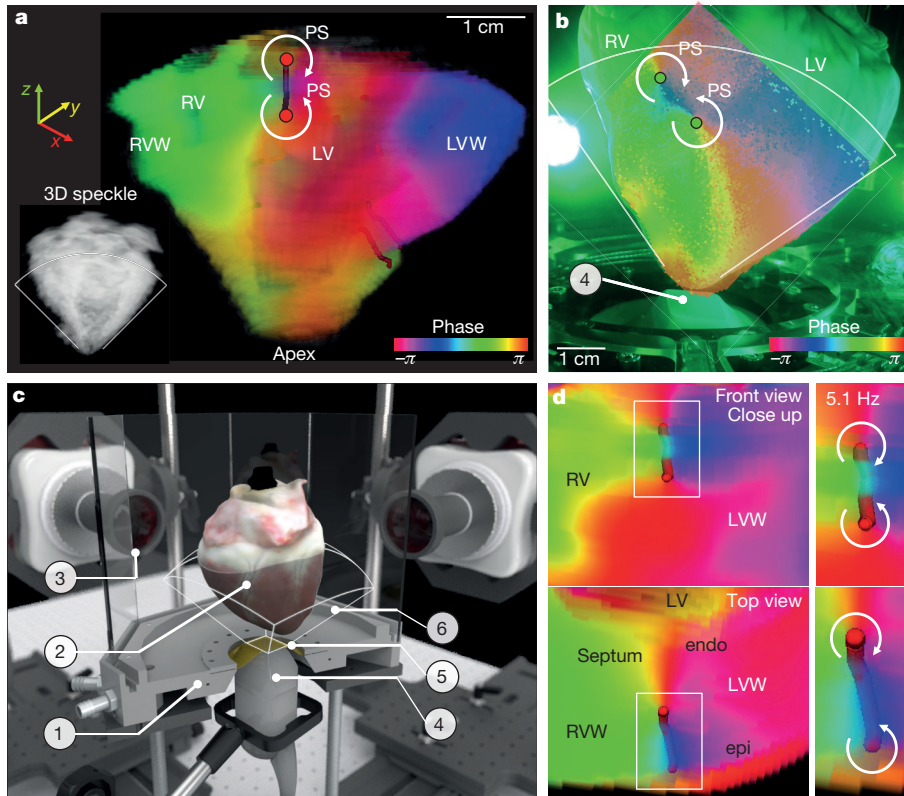


**Figure 1 | Measurement of intramural mechanical filament-like phase singularity.** **a**, Double scroll wave (phase) and U-shaped mechanical filament (red) recorded at 134 volumes per second during ventricular tachycardia inside the left ventricular wall (LVW) of a contracting Langendorff-perfused pig heart using 4D ultrasound (Supplementary Video 1 and Extended Data Fig. 1 a, b). LV, left ventricle; RV, right ventricle; RVW, right ventricular wall; PS, phase singularity. **b**, Figure-of-eight spiral wave (membrane voltage) on the surface of the left and right ventricle with two phase singularities obtained by recording

optical mapping data at the same time as the recording shown in **a**. The ultrasound transducer is indicated by (4); the white lines indicate the field of view. **c**, Schematic of the experimental setup. (1) temperature-controlled perfusion bath; (2) Langendorff-perfused pig heart; (3) high-speed EMCCD (electron-multiplying charge-coupled device) cameras (only two shown) and LED illumination (not shown); (4) 4D ultrasound transducer; (5) acoustic window (membrane); (6) 3D field of view of ultrasound transducer. See the Methods for details. **d**, Detail (front and top view) of the U-shaped mechanical filament (red) of the scroll wave shown in **a**.

(Fig. 2a and Extended Data Fig. 9c). In general, we found that the cardiac muscle exhibits deformations during cardiac fibrillation<sup>20</sup> that retain vortex-like patterns and, like fingerprints of electrical vortex activity, reveal the topological organization of cardiac fibrillation throughout the heart wall. Furthermore, we found that rotational centres of the mechanical rotor patterns can be displayed as phase singular points or filament-like lines of phase singularity, as has been shown previously for electrical activity<sup>12,13</sup> (see Supplementary Videos 1, 2, 6–8, 11).

To further elucidate the dynamics of electrical and mechanical vortex filaments, we conducted computer simulations of scroll waves in excitable and contractile cardiac tissue (see Methods). Figure 2c, d show simulation data of electromechanical vortex filament dynamics using realistic heart geometry and fibre orientation. Our simulations indicate that electromechanical turbulence in the heart is composed of entangled pairs of co-existing electromechanical vortex filaments. The filaments emerge in close vicinity to each other due to electromechanical coupling (Supplementary Video 3). The simulations suggest that the experimentally observed mechanical filaments inside the ventricular wall may be intrinsic dynamical entities that can be used to characterize the spatiotemporal organization of cardiac fibrillation.

To investigate the dynamics and interaction of electrical and mechanical rotors experimentally, we have developed a multi-modal fluorescence imaging system, which allows for the simultaneous measurement of membrane voltage, intracellular calcium and mechanical strain on the surface of the heart (Fig. 3b–d). Standard optical mapping is very sensitive to mechanical motion of tissue, which may result in

substantial distortions of the signal. To avoid these motion artefacts<sup>21</sup>, pharmacological excitation–contraction uncoupling agents have been applied in previous experiments to inhibit any contractile motion of the heart. By contrast, we used computer vision techniques to disentangle fluorescence signals (voltage, calcium) from mechanical deformation, which not only overcomes the limitations imposed by motion artefacts<sup>22–26</sup>, but also enables quantitative motion analysis (Supplementary Videos 4, 5). Figure 3b illustrates the marker-free motion-tracking algorithm. The algorithm estimates the displacement of the epicardial surface from a reference configuration to its instantaneous configuration at any subsequent time  $t$ . This transformation of coordinates is used to convert the fluorescence signal from the stationary camera frame of reference into the co-moving frame of reference. Within the co-moving frame of reference, fluorescence signals are essentially artefact-free. The efficacy and quality of the motion tracking may be assessed from the examples shown in Fig. 3c. The original fluorescence data show that the signal is substantially distorted by tissue motion, rendering a quantitative analysis impossible. However, within the co-moving reference frame, artefacts are significantly reduced, allowing the voltage and calcium signals to be reliably retrieved. Simultaneously, non-rigid motion tracking provides a measurement of the tissue coordinates and local deformation of the cardiac tissue as a function of time. An example of a simultaneous measurement of membrane voltage, calcium and the corresponding strain rate is shown in Fig. 3d (Supplementary Video 8). The time series show that the tissue experiences deformations that correlate with the sequence of electrical activation.

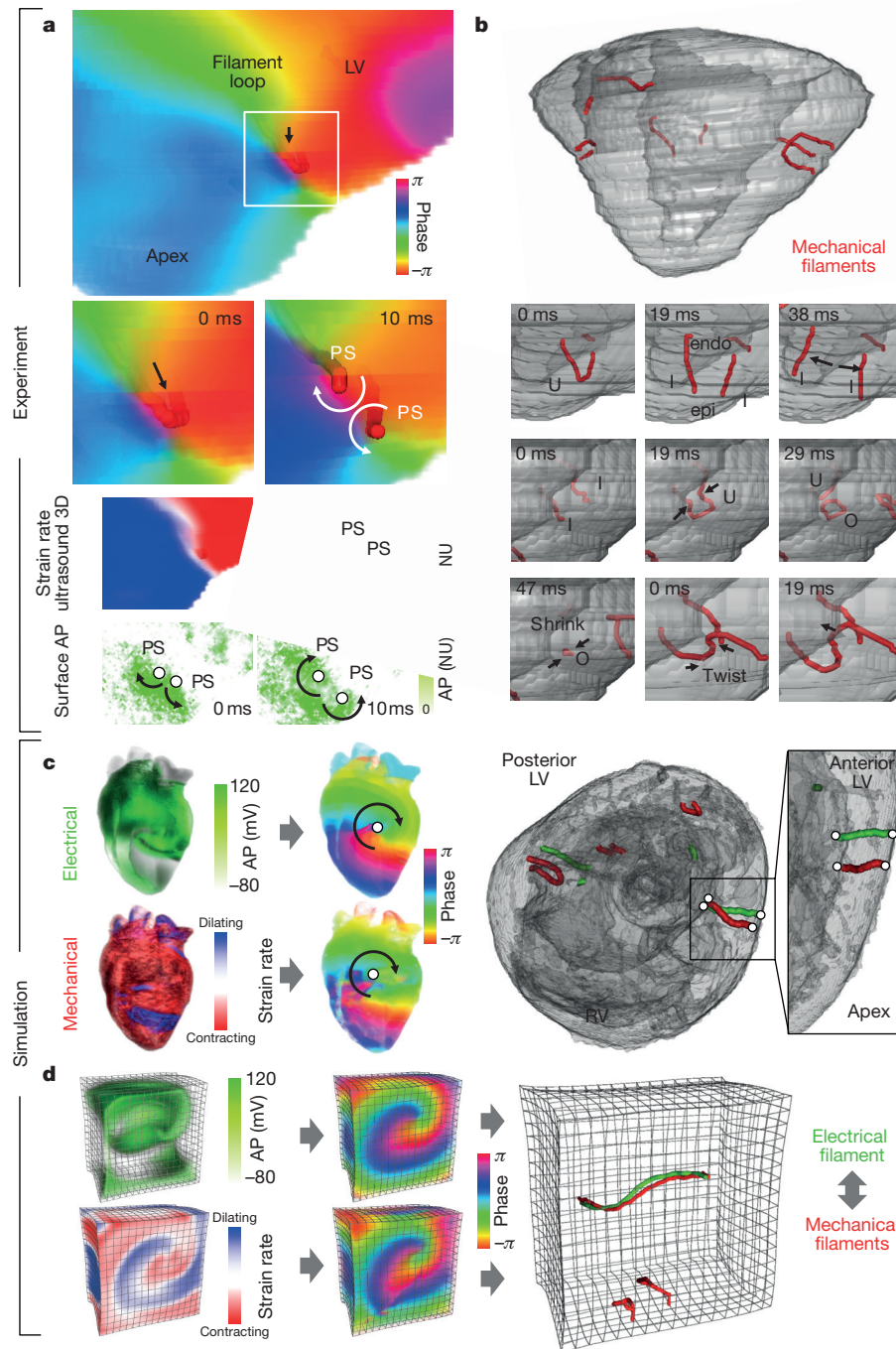


**Figure 2 | Electromechanical phase singularity in the experiments and simulations.** **a**, Breakthrough of the U-shaped intramural mechanical filament (red) on the epicardial surface (LVW, pig) results in the formation of two transmural filaments during ventricular fibrillation and two phase singularities (circles) with opposite charges (counter-rotating spirals) on the surface. Optical mapping (voltage and strain rate) confirms the breakthrough of filament that is observed with 4D ultrasound (Supplementary Video 2). **b**, Creation and extinction of mechanical filaments (red) inside pig ventricles (grey shaded) between endocardial

(endo) and epicardial (epi) heart surface during ventricular fibrillation imaged using 4D ultrasound. Snapshots show interaction and transition of I-, U-, and O-shaped filaments. **c**, **d**, Numerical simulation of electrical (green, action potential (AP)) and mechanical (red–blue: strain rate with contracting (red) and dilating (blue) rates of deformation) scroll waves in the rabbit heart (computed tomography scan) and rectangular bulk with associated electrical (green) and mechanical (red) vortex filaments (Supplementary Video 3). NU, normalized units.

Applying this optical mapping system to ventricular fibrillation, we observed simultaneously co-localized rotors in the action potential, calcium and strain measurements (Fig. 3e, f) on the surface of intact Langendorff-perfused rabbit hearts (Supplementary Videos 6–8). The coupling of cardiac excitation and contraction (Fig. 3a) may result in a mechanical rotor, which consists of two adjacent regions of dilating and contracting strain rates rotating around each other (see

also Extended Data Fig. 4a–c). Analogous to electrical rotors, mechanical rotors are characterized by a phase singularity, indicating the centre of rotation. In order to investigate the spatiotemporal organization of electrical and mechanical rotors, data and statistical analyses were obtained in rabbit ( $n = 3$ ) and pig hearts ( $n = 3$ ). During ventricular fibrillation, the position of electrical and mechanical rotors were calculated and tracked over time. In total, 3,180 trajectories of phase

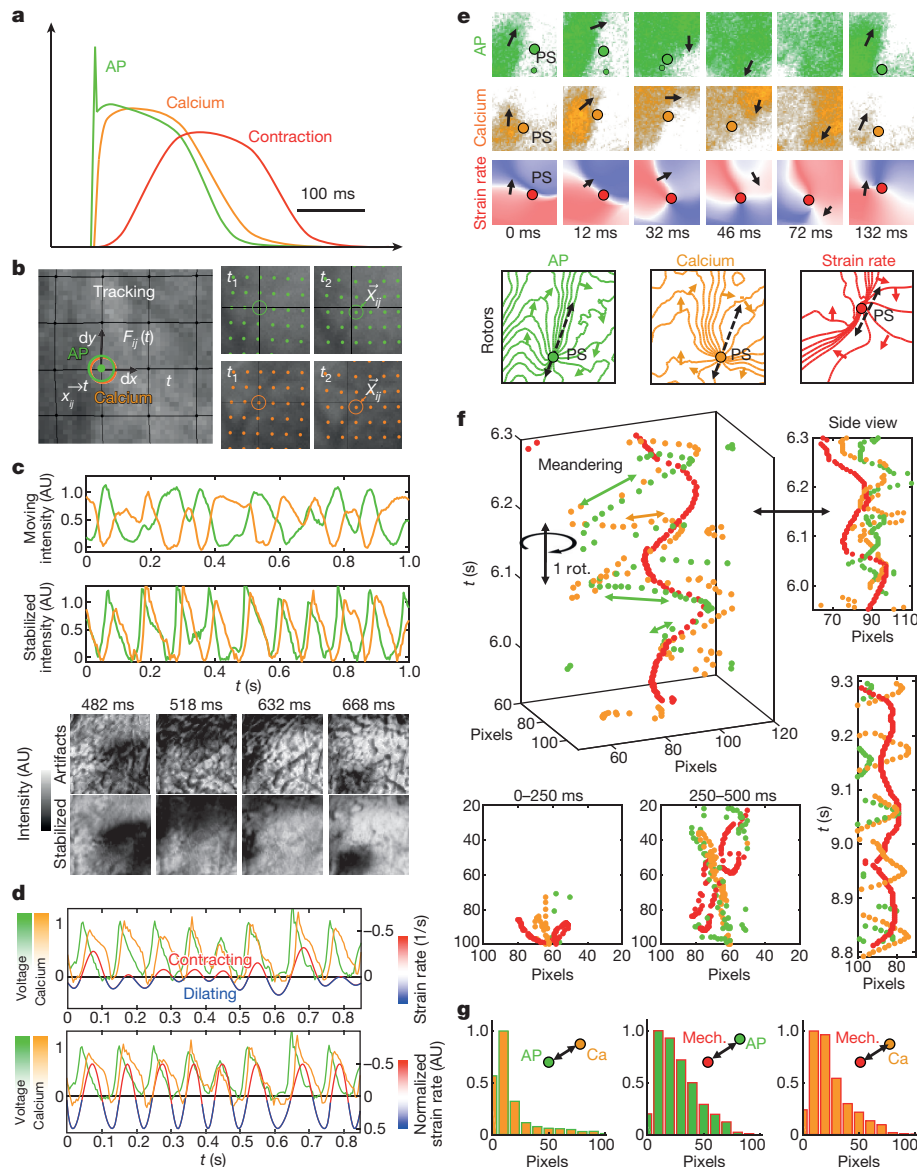


**Figure 3 | Optical mapping of electromechanical phase singularities during ventricular fibrillation**<sup>28</sup> in the cardiomyocyte. **a**, Excitation–contraction coupling<sup>28</sup> in the cardiomyocyte. Action potentials (AP, green) trigger the release of intracellular calcium (orange), resulting in cellular contraction (red). **b**, Numerical motion tracking in optical mapping data disentangles mechanical motion (deformation) from voltage and calcium signals. **c**, Efficacy of numerical motion tracking and motion-artefact removal. Top graph, without motion tracking, the time-series shows artefacts. Bottom graph, action potentials and calcium measured on the contracting heart surface after motion tracking. Top image sequence, the non-tracked action potential wave shows substantial motion artefacts (with a high frequency spatial pattern). Bottom image sequence, after motion tracking, a spiral wave (action potential, dark indicates depolarized tissue) is revealed (Supplementary Videos 4, 5 and Extended Data Fig. 4a). **d**, Simultaneous measurement of action potentials, calcium and deformation during ventricular fibrillation using optical mapping.

singularities (electrical and mechanical) were measured in pig hearts, and 1,142 trajectories of phase singularities were measured in rabbit hearts. Along these trajectories, the positions of the phase singularities were sampled at 250 or 500 Hz. Representative trajectories of the electrical and mechanical phase singularities ( $x$ – $y$ – $t$  plots) are shown in Figs 3f, 4f (rabbit) and Fig. 4a–c (pig). From these trajectories, basic statistical information has been retrieved (Figs 3g, 4d and Extended Data Fig. 6a–d).

Repetitive electrical activation leads to a corresponding sequence of dilating (blue indicates strain rates  $<0$ ) and contracting (red indicates strain rates  $>0$ ) rates of deformation. Top, raw unnormalized strain rate signal containing amplitude variations. Bottom, normalized strain rate used for computing of the phase signal (Extended Data Fig. 4b). **e**, Rotating electrical (voltage and calcium) and mechanical activity during ventricular fibrillation. **f**, Phase singularity space–time plots of action potentials, calcium and mechanics on the ventricular surface. Mechanical phase singularities co-localize with voltage and calcium phase singularities over multiple rotations, even for meandering rotors (1 pixel (px) = 0.16 mm, 100 pixels = approximately the diameter of the heart (16 mm)). **g**, Histogram of distances between phase singularities (voltage-to-calcium, voltage-to-mechanics, calcium-to-mechanics) during ventricular fibrillation shows co-localization with peaks at approximately  $0.8 \pm 0.8$  mm (average distance between phase singularities is  $4.0 \pm 0.8$  mm). AU, arbitrary units.

Our experimental data show that across hearts and species (pig, rabbit) the observed electrical and mechanical phase singularities remain similar in number and lifetime (Fig. 4g, h). The data also support the hypothesis that, on average, electrical phase singularities are associated with nearby mechanical phase singularities, with the average nearest neighbour distance between an electrical and its corresponding mechanical phase singularity being small, compared to the distance to the next electrical or mechanical phase singularity (Fig. 4a–e and Extended Data Table 1).

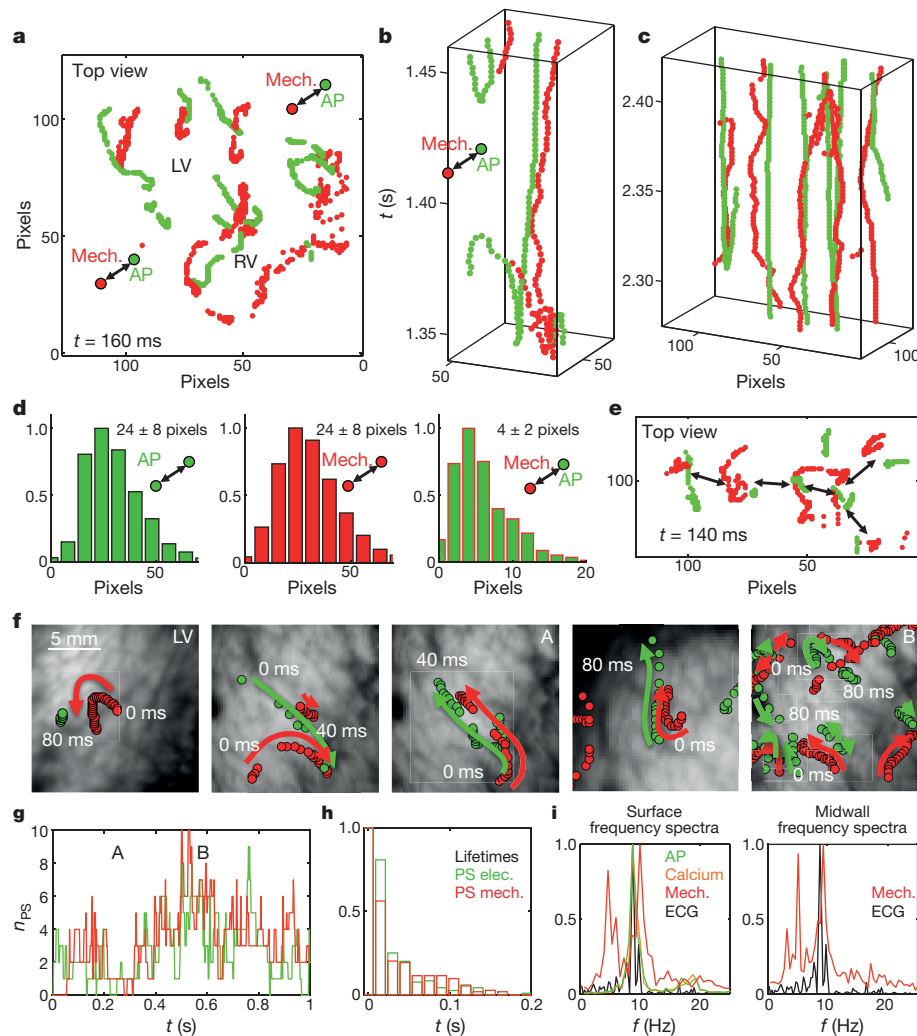


**Figure 4 | Dynamics of electromechanical phase singularity during ventricular fibrillation.** **a–c, e,** Co-localization of epicardial voltage (green) and mechanical (red) phase singularities on the pig heart surface at 160-ms (**a**), 110-ms (**b**), 120-ms (**c**) and 140-ms (**e**) intervals (1 pixel = 0.78 mm). **d,** Histograms of nearest neighbour distances between phase singularities (voltage-to-voltage, mechanics-to-mechanics and voltage-to-mechanics) during ventricular fibrillation (pig). **f,** Phase singularity trajectories within intervals of 40 ms and 80 ms during ventricular fibrillation (rabbit,  $n = 3$ ). **g,** Temporal evolution of electrical

and mechanical phase singularity numbers (rabbit). **f, g,** A and B indicate intervals of low and high phase singularity density, respectively. **h,** Histogram of lifetimes of electrical and mechanical phase singularities (rabbit). **i,** Frequency spectra of voltage, calcium and strain rate on the rabbit heart surface obtained from optical mapping, mechanical deformation (strain rate) within the heart wall obtained from 2D ultrasound and electrocardiogram recordings. Dominant frequencies are  $9 \pm 1$  Hz (Extended Data Figs 4e, 9a–c).

On the cellular level, electrical and mechanical processes in the heart are related through excitation–contraction coupling and mechano-electrical feedback. On the organ level, diffusive coupling of cardiomyocytes allows electrical impulses to propagate as an activation wave, which leads to well-coordinated and relatively uniform mechanical contraction of cardiac tissue in the normal heart. In the diseased heart, excitation–contraction coupling and mechano-electrical feedback may be altered, resulting in contractile dysfunction and onset of arrhythmias. Although electrical and mechanical processes are intrinsically coupled, the physical nature of the emergent electrical and mechanical wave phenomena is very different. Electrical waves in the heart are solitary excitation waves (and, for example, annihilate under collision) with a typical conduction velocity of  $1 \text{ m s}^{-1}$ . By contrast, electromechanical waves<sup>27</sup> are elastic deformation waves, which are initiated by the excitation waves via excitation–contraction coupling. However, their wave-like propagation may be altered owing to subsequent interactions between the mechanically interconnected physiological structures of the heart. Passive elastic waves travelling through the heart also have the potential to effectively introduce non-local mechanical interactions because of the large speed of sound

(approximately  $1,500 \text{ m s}^{-1}$ ) in cardiac tissue. Although our results for ventricular fibrillation and ventricular tachycardia provide evidence for coupling of the voltage and calcium dynamics (Extended Data Fig. 5), coupled electromechanical dynamics and the coexistence of electrical and mechanical phase singularities, elastic patterns should not be considered as a simple proxy for the underlying electrical activation. Consequently, we expect that the mutual coupling of electrical and mechanical waves in a deformable excitable medium, such as the heart, gives rise to very rich spatiotemporal dynamics that still need to be explored (Supplementary Video 12, Extended Data Figs 7, 8 and Supplementary Discussion). Despite their complex interactions, electrical and mechanical phase singularities show similar properties, including topological charge, structure, dynamics and lifetime, suggesting that the spatiotemporal dynamics of the electrical and mechanical system are essentially two sides of the same coin.

We believe that the imaging approach introduced in this study will provide the basis for the integrative study of these electromechanical phenomena (such as excitation–contraction coupling and mechano-electrical feedback) at the tissue and organ level in health and disease. We expect that these developments will help to unravel the mechanisms

that underlie the spatiotemporal organization of electromechanical turbulence during cardiac fibrillation and could lead to safer and more effective diagnostic and therapeutic clinical applications.

**Online Content** Methods, along with any additional Extended Data display items and Source Data, are available in the online version of the paper; references unique to these sections appear only in the online paper.

**Received 14 December 2016; accepted 14 February 2018.**

**Published online 21 February 2018.**

1. Welsh, B. J., Gomatam, J. & Burgess, A. E. Three-dimensional chemical waves in the Belousov–Zhabotinskii reaction. *Nature* **304**, 611–614 (1983).
2. Rotermund, H. H., Engel, W., Kordesch, M. & Ertl, G. Imaging of spatio-temporal pattern evolution during carbon monoxide oxidation on platinum. *Nature* **343**, 355–357 (1990).
3. Huang, X. *et al.* Spiral waves in disinhibited mammalian neocortex. *J. Neurosci.* **24**, 9897–9902 (2004).
4. Winfree, A. T. Scroll-shaped waves of chemical activity in three dimensions. *Science* **181**, 937–939 (1973).
5. Fenton, F. & Karma, A. Vortex dynamics in three-dimensional continuous myocardium with fiber rotation: filament instability and fibrillation. *Chaos* **8**, 20–47 (1998).
6. Clayton, R. H., Zhuchkova, E. A. & Panfilov, A. V. Phase singularities and filaments: simplifying complexity in computational models of ventricular fibrillation. *Prog. Biophys. Mol. Biol.* **90**, 378–398 (2006).
7. Winfree, A. T. Electrical turbulence in three-dimensional heart muscle. *Science* **266**, 1003–1006 (1994).
8. Krinsky, V. I. Spread of excitation in an inhomogeneous medium (state similar to cardiac fibrillation). *Biofizika* **11**, 676–683 (1966).
9. Davidenko, J. M., Pertsov, A. V., Salomonsz, R., Baxter, W. & Jalife, J. Stationary and drifting spiral waves of excitation in isolated cardiac muscle. *Nature* **355**, 349–351 (1992).
10. Gray, R. A. *et al.* Mechanisms of cardiac fibrillation. *Science* **270**, 1222–1223 (1995).
11. Jalife, J. & Gray, R. Drifting vortices of electrical waves underlie ventricular fibrillation in the rabbit heart. *Acta Physiol. Scand.* **157**, 123–132 (1996).
12. Gray, R. A., Pertsov, A. M. & Jalife, J. Spatial and temporal organization during cardiac fibrillation. *Nature* **392**, 75–78 (1998).
13. Witkowski, F. X. *et al.* Spatiotemporal evolution of ventricular fibrillation. *Nature* **392**, 78–82 (1998).
14. Fenton, F. H. *et al.* Termination of atrial fibrillation using pulsed low-energy far-field stimulation. *Circulation* **120**, 467–476 (2009).
15. Luther, S. *et al.* Low-energy control of electrical turbulence in the heart. *Nature* **475**, 235–239 (2011).
16. Janardhan, A. H. *et al.* A novel low-energy electrotherapy that terminates ventricular tachycardia with lower energy than a biphasic shock when antitachycardia pacing fails. *J. Am. Coll. Cardiol.* **60**, 2393–2398 (2012).
17. Mitrea, B. G., Caldwell, B. J. & Pertsov, A. M. Imaging electrical excitation inside the myocardial wall. *Biomed. Opt. Express* **2**, 620–633 (2011).
18. Mitrea, B. G., Wellner, M. & Pertsov, A. M. Monitoring intramyocardial reentry using alternating transillumination. *Conf. Proc. IEEE Eng. Med. Biol. Soc.* **2009**, 4194–4197 (2009).
19. Baxter, W. T., Mironov, S. F., Zaitsev, A. V., Jalife, J. & Pertsov, A. M. Visualizing excitation waves inside cardiac muscle using transillumination. *Biophys. J.* **80**, 516–530 (2001).
20. Wiggers, C. J. The mechanism and nature of ventricular fibrillation. *Am. Heart J.* **20**, 399–412 (1940).
21. Svrcek, M., Rutherford, S., Chen, A. Y. H., Provaznik, I. & Smaill, B. Characteristics of motion artifacts in cardiac optical mapping studies. *Conf. Proc. IEEE Eng. Med. Biol. Soc.* **2009**, 3240–3243 (2009).
22. Rohde, G. K., Dawant, B. M. & Lin, S. F. Correction of motion artifact in cardiac optical mapping using image registration. *IEEE Trans. Biomed. Eng.* **52**, 338–341 (2005).
23. Seo, K. *et al.* Structural heterogeneity in the ventricular wall plays a significant role in the initiation of stretch-induced arrhythmias in perfused rabbit right ventricular tissues and whole heart preparations. *Circ. Res.* **106**, 176–184 (2010).
24. Bourgeois, E. B., Bachtel, A. D., Rogers, J. M., Huang, J. & Walcott, G. P. Simultaneous optical mapping of transmembrane potential and wall motion in isolated, perfused whole hearts. *J. Biomed. Opt.* **16**, 096020 (2011).
25. Zhang, H., Iijima, K., Huang, J., Walcott, G. P. & Rogers, J. M. Optical mapping of membrane potential and epicardial deformation in beating hearts. *Biophys. J.* **111**, 438–451 (2016).
26. Christoph, J., Schröder-Schetelig, J. & Luther, S. Electromechanical optical mapping. *Prog. Biophys. Mol. Biol.* **130**, 150–169 (2017).
27. Provost, J., Lee, W.-N., Fujikura, K. & Konofagou, E. E. Imaging the electromechanical activity of the heart in vivo. *Proc. Natl Acad. Sci. USA* **108**, 8565–8570 (2011).
28. Bers, D. M. Cardiac excitation–contraction coupling. *Nature* **415**, 198–205 (2002).

**Supplementary Information** is available in the online version of the paper.

**Acknowledgements** We thank U. Parlitz and N. Otani for discussions, M. Kunze, D. Hornung and U. Schminke for technical assistance, L. Bess for linguistic advice and FujiFilm VisualSonics Inc. and Siemens HealthCare for their technical support. This work was supported by the German Ministry for Education and Research through FKZ O31A147 (S.L.); by the German Center for Cardiovascular Research (S.L. and G.H.); by the German Research Foundation through SFB 1002 Modulatory Units in Heart Failure (S.L., J.C. and G.H.) and SFB 937 Collective Behavior of Soft and Biological Matter (S.L. and J.C.); by the National Science Foundation (NSF) grants 1341190 and 1413037 (F.H.F.); by the American Heart Association (AHA) grant 15POST25700285 (I.U.); by the Human Frontiers Science Program through fellowship LT000840/2014-C (P.B.) and by the Max Planck Society.

**Author Contributions** J.C. and S.L. designed research and wrote the paper with F.H.F., G.H., P.B. and R.F.G.; J.C., S.L. and J.S.-S. designed the experiments; I.U. and F.H.F. contributed to the experimental setup; J.C. performed the experiments and analysed the data; M.C., J.S.-S., C.R., I.U. and F.H.F. contributed to the experiments; J.C., P.B. and S.S. provided the numerical simulations. All authors read and approved the manuscript.

**Author Information** Reprints and permissions information is available at [www.nature.com/reprints](http://www.nature.com/reprints). The authors declare competing interests: details are available in the online version of the paper. Readers are welcome to comment on the online version of the paper. Publisher's note: Springer Nature remains neutral with regard to jurisdictional claims in published maps and institutional affiliations. Correspondence and requests for materials should be addressed to J.C. ([jan.christoph@ds.mpg.de](mailto:jan.christoph@ds.mpg.de)) and S.L. ([stefan.luther@ds.mpg.de](mailto:stefan.luther@ds.mpg.de)).

**Reviewer Information** *Nature* thanks A. Holden, J. Jalife, E. Konofagou and the other anonymous reviewer(s) for their contribution to the peer review of this work.

## METHODS

**Data reporting.** No statistical methods were used to predetermine sample size. The experiments were not randomized and the investigators were not blinded to allocation during experiments and outcome assessment.

**Animal ethics.** All procedures regarding care and use of animals were solely performed by appropriately trained personnel and were in accordance with German animal welfare laws and were reported to the local animal welfare representatives. Pre-experimental handling and humane welfare-oriented procedures strictly followed the regulations for animal welfare, in agreement with German legislation, local stipulations and in accordance with recommendations of the Federation of European Laboratory Animal Science Associations (FELASA). All involved scientists and technicians have been accredited by the responsible ethics committee (the Lower Saxony State Office for Customer Protection and Food Safety—LAVES).

**Ex vivo electromechanical imaging.** Experiments were conducted in isolated, intact Langendorff-perfused pig ( $n = 5$ ) and rabbit ( $n = 5$ ) hearts. Ventricular fibrillation and ventricular tachycardia were induced using rapid pacing<sup>14,15</sup>. Hearts were simultaneously imaged at high speeds using optical fluorescence (optical mapping) and ultrasound imaging.

**Optical fluorescence imaging.** Fluorescence imaging was performed using either a panoramic imaging setup with 4 high-speed cameras (pig, together with 4D ultrasound) imaging voltage only (mono-parametric) or a monocular single-camera setup (rabbit, together with 2D ultrasound) filming voltage and calcium simultaneously (multi-parametric), as previously described<sup>29</sup>. Imaging was performed at a frame rate of 500 Hz with a spatial resolution of 0.16–0.78 mm with 2–10-cm fields of view with high-speed EMCCD cameras (Evolve, 128 × 128 pixels, Photometrics) together with high-numerical-aperture lenses (pig: 9 mm, f1–1.4, Fujinon; rabbit: 52 mm, f0.95–1.6, Tokina). Hearts were imaged from the side through the glass walls of an eight-sided aquarium at a distance of about 20.0–40.0 cm. During mono-parametric imaging of voltage, green excitation light was provided by up to 12 high-performance light-emitting diodes (LEDs, 532 nm ± 10 nm centre wave length). During multi-parametric imaging of voltage and calcium, two sets of high-performance LEDs (three green and three red LEDs, LZ4-G40-100 and LZ4-R40-100, LED Engin; filtered at 550 ± 5 nm and 640 ± 5 nm) were switched rapidly (500 Hz) using a custom-made fast-switching diode driver box (I.U. and F.H.F., Georgia Institute of Technology), resulting in an effective frame rate of 250 Hz for voltage and calcium recordings, respectively. Emission light was filtered using red/near-infrared longpass or bandpass filters (mono-parametric imaging, longpass filter with transmission > 610 nm; multi-parametric imaging, dual-bandpass filter with transmission bandwidths at 585 nm and 800 nm, ET585/50 nm and 800/200 nm; Chroma Technologies). In mono-parametric imaging mode, the tissue was stained with a voltage-sensitive dye (Di-4-ANEPPS, 20 ml of 1 mMol l<sup>-1</sup> concentrated dye in Tyrode solution). In multi-parametric imaging mode, the tissue was stained with a voltage-sensitive dye (Di-4-ANBDQPB, 40 μl bolus injection of 24.4 mg ml<sup>-1</sup> concentrated dye in ethanol) and a calcium-sensitive dye (Rhod2-AM, 500 μl and 4.5 ml Tyrode solution over 5 min injected into the bubble trap). Pharmacological excitation–contraction uncoupling substances were not used. Cameras were triggered externally (20 MHz Function/Waveform Generator, 33220A, Agilent) and trigger signals were captured using a data-acquisition system (MP150/AcqKnowledge, Biopac Systems Inc.). Movies were acquired using custom-made recording software (MultiRecorder, version 2.0.9, Research Group Biomedical Physics, Max Planck Institute for Dynamics and Self-Organization).

**Motion tracking, motion compensation and strain analysis in fluorescence video data.** The heart's motion was tracked using Lucas–Kanade optical flow estimation algorithms<sup>30–32</sup>. The contrast in the video data was enhanced to facilitate motion tracking, as previously described<sup>26</sup>. The tissue's mechanical configuration was tracked in every pixel throughout the sequence of images with respect to one selected reference frame. The resulting time-varying, two-dimensional displacement vector fields were stored for further processing and erroneously tracked displacements were determined by computing the deviations of the vectors in a small neighbourhood of pixels (3–5 pixels diameter) and outliers were removed based on a threshold value ( $tr = 5.0$  accumulated length in pixels) or by removing individual vectors with lengths that exceeded a threshold value ( $tr = 4.0$  pixels). The missing vectors (less than 5%) were substituted by a vector interpolated from the remaining surrounding displacement vectors (within 5–7 pixels diameter). The resulting time-varying vector field was smoothed in space and over time using spatiotemporal filter kernels with a Gaussian profile (diameter  $d = 3–5$  pixels, 5–7 frames linear averaging). To obtain the instantaneous displacements between two subsequent frames, each frame was subtracted from the previous frame. The resulting time-varying vector field of instantaneous displacements was smoothed in space and over time using spatiotemporal filter kernels with a Gaussian profile (radius  $r = 20–30$  pixels, 5–11 frames linear averaging). From the smoothed vector field the gradient deformation tensors and the Green–Lagrangian strain tensors were computed. The data of the tensors were reduced to scalar-valued

data calculating tensor invariants, that is, the tensor trace, principal stretches or eigenvalues. The strain invariant (tensor trace) was normalized using sliding-window normalization as shown in Fig. 3d or Extended Data Fig. 4b, with a window width  $w$  of at least  $1 \times$  the period of the dominant frequency and typically not more than 1.5–2.5 periods of the dominant frequency. The resulting time-varying strain rate map was smoothed in space and over time using spatiotemporal filter kernels with a Gaussian profile ( $d = 5$  pixels, 7 frames linear averaging). Warped, motion-stabilized videos were created using the evolution of the tracked tissue configurations to redistribute the intensity distribution of each pixel from the current frame along the inversely shifted direction to the tissue configuration of the reference frame. Pixel values were resampled into a regular pixel grid corresponding to the reference configuration using polygon clipping. All computational routines for extraction, processing and visualization of the fluorescence imaging data were custom-made routines written in C/C++ and OpenGL.

**Ultrasound imaging.** Ultrasound imaging was performed either with a 4D ultrasound probe (4Z1c, matrix-array transducer, 2.8 Mhz centre frequency) and system (Acuson sc2000, Siemens AG) in pig hearts, or a 2D cross-sectional probe (MS-550D, linear array transducer, 22–55 MHz broadband frequency) and system (Vevo 2100, FUJIFILM Visualsonics Inc.) in rabbit hearts. 4D imaging refers to the acquisition of 3D volume images over time ( $3D + t$ ). 2D imaging refers to the acquisition of 2D images over time ( $2D + t$ , B-mode). The 4D probe produces volume frames with a pyramid shape (maximum opening angle  $90 \times 90$  degrees, 6–14 cm lateral depth or pyramid height) and a relatively coarse spatial resolution (approximately 100 voxels<sup>3</sup>) but large fields of views (approximately  $3 \times 6 \times 6$  cm<sup>3</sup> to  $10 \times 10 \times 6$  cm<sup>3</sup>) at volume frame rates ranging from 51 volumes per second to 188 volumes per second depending on the lateral depth and opening angle of the pyramid (see Supplementary Table 1 for details). The spatial resolution is approximately 0.5 mm<sup>3</sup> and decreases with the lateral distance from the transducer. The probe was positioned below an acoustic window (latex membrane) centred at the bottom of the tissue bath (Fig. 1c). A transducer mounting system (custom-made mounting arm based on dial indicator holder arm, Hoffmann Group) allowed arbitrary alignment of the imaging field of view (around several axes) and to secure the transducer in a stationary position once the desired imaging position and alignment was found. The field of view of the ultrasound imaging was facing upwards, covering the ventricles of the pig heart (Fig. 1b, c). The entire ventricular walls were imaged at a temporal resolution of 5.3–11.8 ms (6–10 cm lateral field of view, 85–188 volumes per second). With a reduced field of view (that is,  $36^\circ \times 90^\circ$  to  $50^\circ \times 90^\circ$ ), the entire left ventricular wall was imaged at a temporal resolution of 5.3–7.5 ms (134–188 volumes per second). The sampling distance during high-speed 4D imaging was reduced to enhance imaging speeds (T2 pre-setting from manufacturer). The 2D probe produces high-resolution ( $13 \mu\text{m}$  in lateral and  $27 \mu\text{m}$  in transversal direction) cross-sectional (B-mode) ultrasound speckle images. Imaging was performed at low line densities (pre-setting: 128 lines) at frame rates ranging from 279 to 309 frames per second with fields of views ranging in the order of approximately  $1 \text{ cm} \times 1 \text{ cm}$  and the frame rate varying with B-mode image widths and depths (see Supplementary Table 1 for details). The probe was inserted into the bath from the top facing the bottom of the aquarium. Hearts were imaged with the 2D imaging plane embedded within the left ventricular wall, intersecting the wall tangentially approximately at midwall. A transducer mounting system allowed arbitrary alignment of the field of view (around several axes) and fixing the transducer in a stationary position. The imaging plane normally approximately coincided with the optical axis of the fluorescence imaging setup. Ultrasound TTL-trigger signals were captured using a data-acquisition system and software (MP150/AcqKnowledge, Biopac Systems Inc.), to be able to synchronize the start of the recording with other acquired data.

**Ultrasound data post-processing.** 2D and 3D ultrasound movies were acquired in RF-format (proprietary formats from manufacturers, FUJIFILM Visualsonics Inc. and Siemens AG) and saved as 3D and 4D arrays (custom binary format, 8-bit brightness mode, speckle intensities as integer values ranging from 0 to 255). The arrays were then converted to 32-bit floating point data containing the normalized speckle intensities (ranging from 0 to 1), the intensity values being normalized by the maximal and minimal speckle intensity values in the entire array (or entire recording or part of the recording). 3D speckle images were resampled (custom-made python routine, using VTK-ProbeFilter resampling filter, VTK Visualization Toolkit, Kitware Inc.) from a pyramid-shaped image format into a Cartesian image format with a regular voxel grid structure with grid sizes in the order of  $100 \times 100 \times 100$  voxels. The height of the pyramid corresponds approximately to one of the lengths of the box. 2D speckle image sizes were in the order of  $500 \times 500$  pixels and typically reduced in size to about  $300 \times 300$  pixels.

**Motion tracking and strain analysis in ultrasound data.** Motion within the volumetric (3D, pig) or cross-sectional (2D, rabbit) ultrasound movie data was tracked using custom-made motion-tracking algorithms<sup>31–33</sup> based on speckle correlation and block-matching. The same algorithm was used for the 2D and 3D

data. Only voxels and pixels showing the heart muscle were considered during the tracking procedure. The image data were segmented into two regions, one showing tissue and one showing the bath (pixel and voxel values: 0 = no tissue, 1 = tissue, ImageJ/Fiji segmentation editor and MATLAB). Ball- (3D) or disk-shaped (2D) blocks or interrogation windows (with diameters of 8–12 voxels and 16–22 pixels) were used to determine shifts of the tissue (within a radius of  $r = 4$  voxels and 10 pixels) in the image data and associate the positions of shifted tissue regions in between two frames. The displacements were determined by minimizing the mean quadratic difference (or absolute difference) of two blocks from two consecutive frames. Sub-pixel displacement accuracy was achieved by computing image moments (weight or centroid in 2D or 3D) in the resulting data containing the spatial distribution of mean quadratic differences for given (whole pixel) shifts. The instantaneous displacements between two subsequent frames were then tracked throughout the sequence of images. Despite the noisy speckle image data, tracking was found to detect a coherent displacement field indicating the shifts of the tissue robustly with few outliers. The resulting time-varying, two- or three-dimensional displacement vector fields containing the shifts of the tissue from one (volume) frame to the next were stored and erroneously tracked displacements were determined by computing the deviations of the vectors in a small (ball- or disk-shaped) neighbourhood of pixels (3–5 voxels or pixels diameter) around each voxel or pixel and outliers were removed based on a threshold value. The missing vectors were substituted by vectors interpolated from the remaining surrounding displacement vectors (within 5–7 voxel or pixel diameter). The resulting time-varying vector field of instantaneous displacements was smoothed in space and over time using spatiotemporal filter kernels with a Gaussian profile (radius  $r = 12$ –16 voxels and 60–80 pixels, 3–5 frames linear averaging). Scalar-valued measures of deformation (tensor invariants, that is, the tensor trace, principal stretches or principal eigenvalues, red–blue colour code with red indicating contractile and blue indicating tensile strain rates) were computed from the gradient deformation tensor and the Green–Lagrangian strain tensor, which were in turn computed from the smoothed displacement vector field. The strain invariant (tensor trace) was normalized using sliding-window normalization with a  $w$  of at least  $1 \times$  the period of the dominant frequency and typically not more than 1.5–2.5 periods of the dominant frequency. The resulting time-varying two- or three-dimensional strain rate map was smoothed in space and over time using spatiotemporal filter kernels with a Gaussian profile ( $d = 7$ –11 voxels or pixels, 3–5 frames linear averaging). All computational routines for extraction, processing and visualization of the ultrasound imaging data were custom-made routines written in C/C++, VTK and OpenGL.

**Computation of phase singularities.** From the amplitude of membrane potential, intracellular calcium, surface and intramural or volume strain, the phase was computed. The phase was computed similarly for both experimental and simulation data using the Hilbert transform. Phase singularities were obtained by computing the line integral<sup>12,13</sup>

$$\oint \nabla \varphi(\mathbf{r}) ds = 2\pi(p - n) \quad (1)$$

where  $\varphi(\mathbf{r})$  is the local phase at a location vector  $\mathbf{r}$  and the integral is taken over the closed path  $s$ .  $p$  and  $n$  are the numbers of positively and negatively charged phase singularities enclosed within the path  $s$ . equation (1) was used previously for the characterization of vortex dynamics during fibrillation<sup>6,12,13,34</sup>. The statistics of electrical and mechanical phase singularities were obtained from  $n = 3$  pig and  $n = 3$  rabbit hearts. Tracking of mechanical phase singularities enabled the reconstruction of the motion and evolution of filaments or phase singular points across space and time. Locations of phase singular points or lines within the moving and deforming medium were stored in the Lagrangian laboratory-coordinate frame.

**Computer simulations.** Computer simulations were performed using realistic heart geometries as well as bulk-shaped geometries. Actively contracting cardiac tissue supporting nonlinear waves of electrical excitation was simulated using electromechanically coupled reaction–diffusion mechanics numerical models<sup>35,36</sup>. The three-variable Fenton–Karma model<sup>5</sup> was used for simulations in realistic, heart-shaped geometries. The two-variable Aliev–Panfilov model<sup>37</sup> was used for simulations in cubic-shaped domains. Parameters for the Fenton–Karma model were set to  $g_{\text{fit}} = 5.6093115$ ,  $\tau_r = 62.41$ ,  $\tau_{\text{si}} = 63.4124$ ,  $\tau_0 = 8.36$ ,  $\tau_{v+} = 10.8037$ ,  $\tau_{v1-} = 40.4284$ ,  $\tau_{v2-} = 36.5891$ ,  $\tau_{w+} = 663.715$ ,  $\tau_{w-} = 132.373$ ,  $u_c = 0.13$ ,  $u_v = 0.05$ ,  $u_{\text{csi}} = 0.45$  with settings for scaling and diffusion properties as previously described<sup>5</sup>. Parameters for the Aliev–Panfilov model were set to  $a = 0.05$ ,  $b = 0.5$ ,  $\mu_1 = 0.1$ ,  $\mu_2 = 0.3$ ,  $\varepsilon = 0.01$ , as previously described<sup>35</sup>. Soft-tissue elasticity was simulated using a discrete particle system with controllable elastic anisotropy, as previously described<sup>32,38</sup>. Bulk-shaped simulation domains consisted of  $80 \times 50 \times 80$  hexahedral cells. Realistic, heart-shaped domains were obtained from computerized tomography scans of the rabbit hearts used in the

experiments by segmenting the voxel data and discretizing the segmented heart-shaped domains into tetrahedral volume elements. The simulation grid typically consisted of  $120 \times 120 \times 120$  simulation grid cells, which each consisted of up to four tetrahedral cells if containing the segmented elastic medium, less than four cells if containing boundaries of the medium, or no cells if situated outside the medium. Electromechanical coupling was realized by introducing a partial differential equation to model excitation-induced active stress build-up, as previously described<sup>35,36,39</sup>. The active stress variable was used to modulate the spring constants of the particle system to model active contractions. However, only springs pointing along the local muscle fibre orientation were modulated, introducing an actively contracting preferred orientation in the elasticity, as well as local transverse isotropy of the passive elasticity<sup>32,38</sup>. The active springs can point into arbitrary directions in the two- or three-dimensional space.

**Time-series and signal analysis.** Frequency power spectra of electrocardiograms and cumulative frequency power spectra of the 2D and 3D experimental data (voltage, calcium, strain rate) and 2D and 3D simulation data (electrical activity, strain rate) were computed using the fast Fourier transform. First, the fast Fourier transform was applied to the entire time-series with typical durations of 2–10 s, with sampling rates of 85–300 Hz (ultrasound), 250–500 Hz (fluorescence imaging) and 2 kHz (electrocardiogram). Next, its absolute square was computed to yield the frequency power spectrum. For spatially extended data (ultrasound, fluorescence imaging and simulations), the calculation was carried out independently for each pixel or voxel, and the resulting spectra were then averaged across the whole spatial domain to yield the cumulative power spectrum.

**Cardiac preparation *ex vivo*.** Göttingen minipigs (female, 21–26 months old,  $45 \pm 3.5$  kg) and New Zealand white rabbits (female, 6–12 months old, 2.5–3.5 kg) were anaesthetized (pig: pentobarbital; rabbit: trapanal) and euthanized via an intravenous injection of potassium chloride (KCl). Immediately after euthanasia, cardioplegic solution was injected intravenously for temporary cessation of cardiac activity. Hearts were excised rapidly and inserted into cardioplegic solution for temporary cessation of cardiac activity. Isolated hearts were transferred quickly into a bath filled with warm, oxygenated (95% O<sub>2</sub> and 5% CO<sub>2</sub>) Tyrode (15 l distilled water, 130 mM sodium chloride (NaCl), 4 mM KCl, 0.6 mM magnesium chloride hexahydrate (MgCl<sub>2</sub>(6H<sub>2</sub>O)), 2.2 mM calcium chloride (CaCl<sub>2</sub>), 1.2 mM sodium dihydrogen-phosphate NaH<sub>2</sub>PO<sub>4</sub>(H<sub>2</sub>O), 24.2 mM sodium bicarbonate (NaHCO<sub>3</sub>) and 12 mM glucose, pH 7.36–7.40) and connected to a retrograde Langendorff-perfusion system (Hugo-Sachs Apparatus). The flow rates of the perfusate were 200 ml min<sup>-1</sup> and 30 ml min<sup>-1</sup> for pig or rabbit hearts, respectively, at a perfusion pressure of  $50 \pm 5$  mm Hg. Tyrode was kept at a constant temperature of  $37 \pm 0.5$  °C (custom-made temperature control, Max Planck Institute for Dynamics and Self-Organization) and was constantly reperfused. Any mechanical pressure to the hearts was avoided to prevent compression of the coronary arteries.

**Arrhythmia induction and termination, data acquisition.** Arrhythmias were induced using rapid pacing via bipolar electrodes or defibrillation paddles, and terminated using a single high-energy cardioversion shock via defibrillation paddles inserted into the bath, if they had not self-terminated, as previously described<sup>14,15</sup>. Electrical power was supplied by a power amplifier (BOB 100-4M, Kepco Power Supply). Electrocardiograms were recorded using three thin electrodes inserted into the bath and acquired using a data-acquisition system (2.0 kHz sampling rate, MP150, Biopac Systems Inc.).

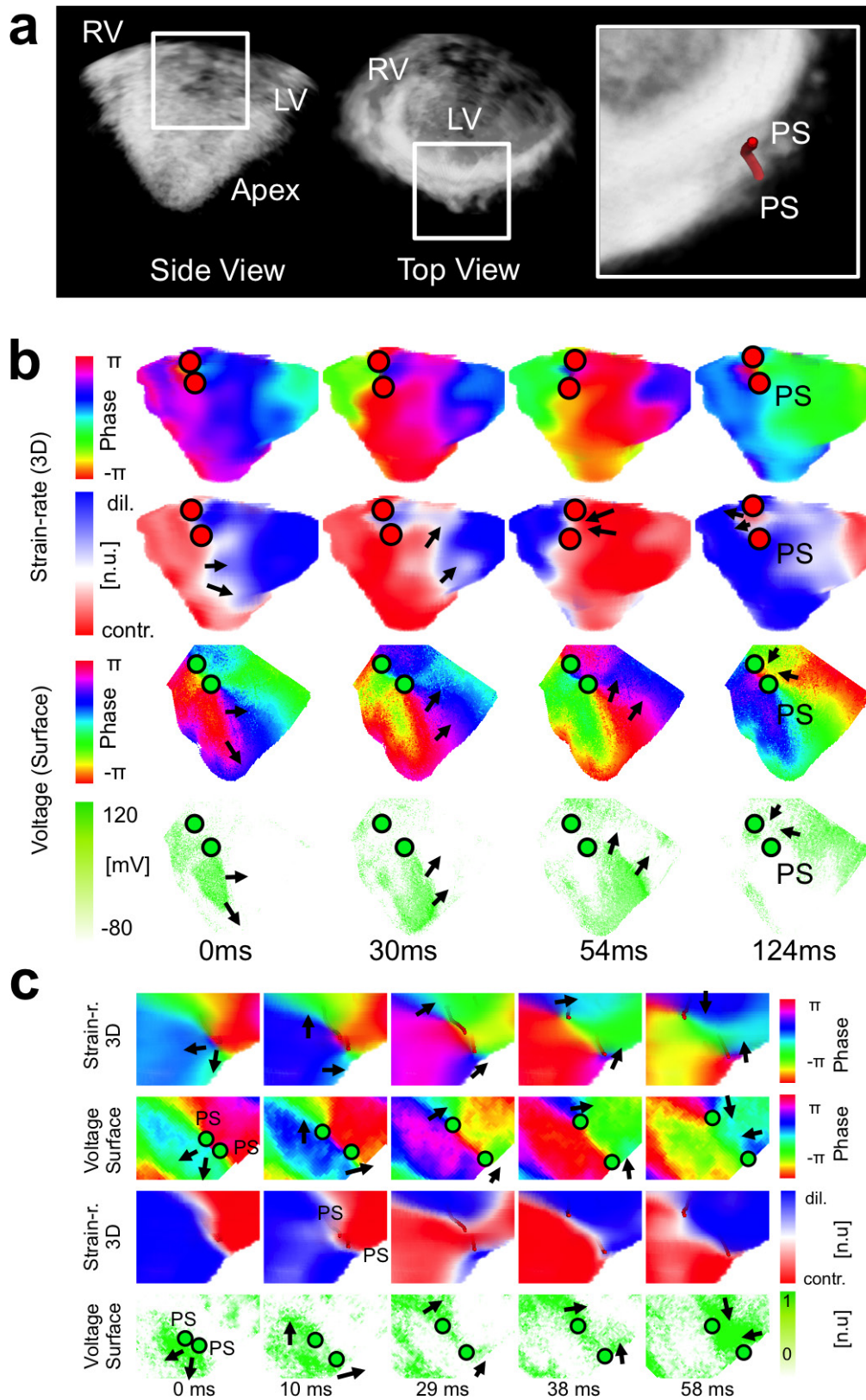
**Computerized tomography scans.** Micro-computed tomography scans of formalin-fixed rabbit hearts were performed using a commercial computerized tomography scanner (GE CT 120, GE Healthcare) operating at  $\mu\text{m}$  spatial resolutions, as previously described<sup>15</sup>. Hearts were fixed immediately after the imaging experiments.

**Code availability.** All custom computer source code used in this study is available from the corresponding author upon reasonable request.

**Data availability.** The datasets generated during and/or analysed during the current study are available from the corresponding author upon reasonable request.

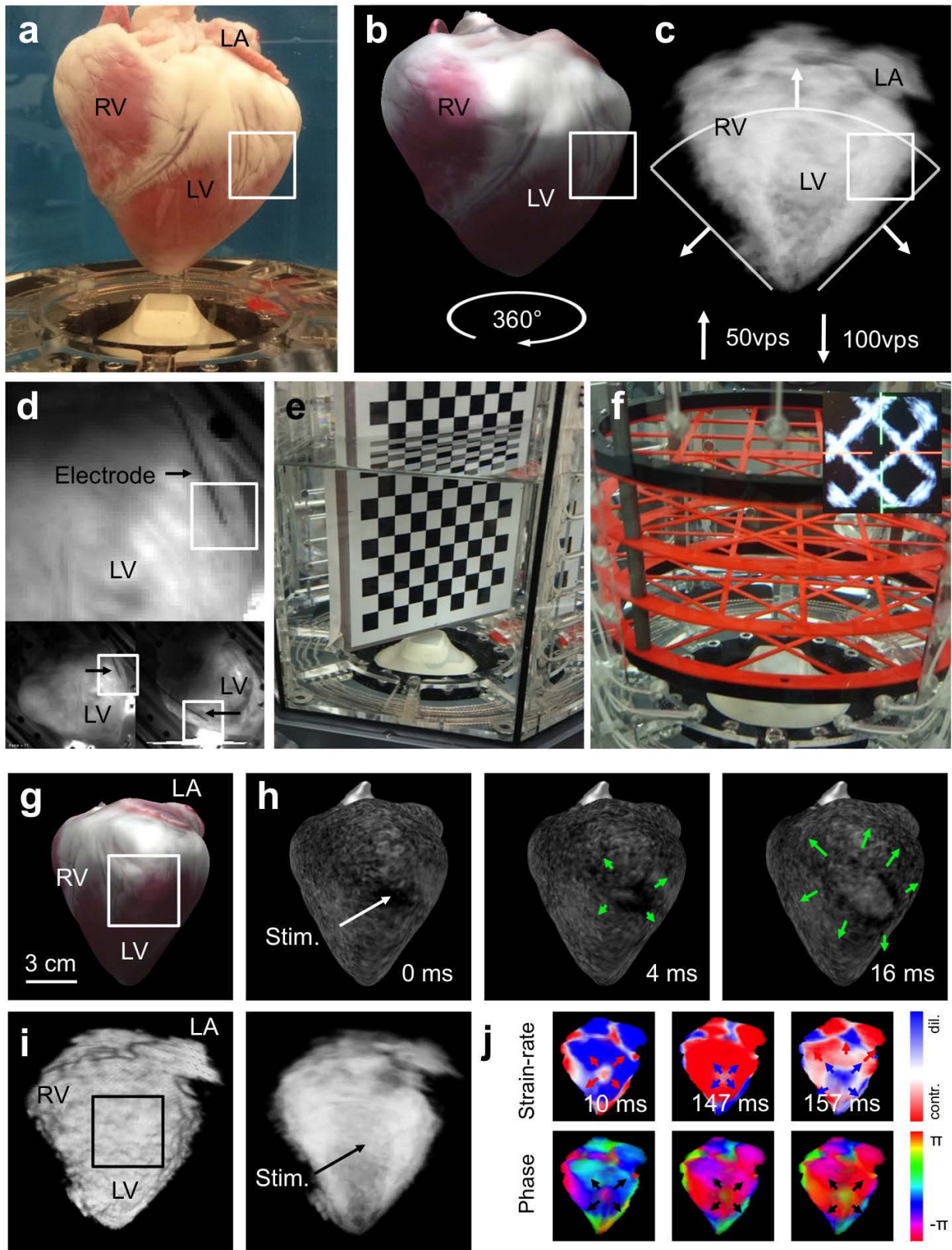
- Lee, P. *et al.* Simultaneous measurement and modulation of multiple physiological parameters in the isolated heart using optical techniques. *Pflugers Arch.* **464**, 403–414 (2012).
- Periaswamy, S., *et al.* H. Differential affine motion estimation for medical image registration. In *Proc. SPIE 4119 Wavelet Applications in Signal and Image Processing VIII* <https://doi.org/10.1117/12.408594> (2000).
- Jakubowski, M. & Pastuszak, S. Block-based motion estimation algorithms — a survey. *Opto. Electron. Rev.* **21**, 86–102 (2013).
- Christoph, J. *Intramural Visualization of Scroll Waves in the Heart*. PhD thesis, Univ. Göttingen (2015).
- Huang, Y.-W., Chen, C.-Y., Tsai, C.-H., Shen, C.-F. & Chen, L.-G. Survey on block-matching motion estimation algorithms and architectures with new results. *J. VLSI Signal Process.* **42**, 297–320 (2006).

34. Pathmanathan, P. & Gray, R. A. Filament dynamics during simulated ventricular fibrillation in a high-resolution rabbit heart. *BioMed Res. Int.* **2015**, 720575 (2015).
35. Nash, M. P. & Panfilov, A. V. Electromechanical model of excitable tissue to study reentrant cardiac arrhythmias. *Prog. Biophys. Mol. Biol.* **85**, 501–522 (2004).
36. Panfilov, A. V., Keldermann, R. H. & Nash, M. P. Drift and breakup of spiral waves in reaction–diffusion–mechanics systems. *Proc. Natl Acad. Sci. USA* **104**, 7922–7926 (2007).
37. Aliev, R. R. & Panfilov, A. V. A simple two-variable model of cardiac excitation. *Chaos Solitons Fractals* **7**, 293–301 (1996).
38. Bourguignon, D. & Cani, M.-P. in *Computer Animation and Simulation* (eds Magnenat-Thalmann, N. *et al.*) 113–123 (Springer, 2000).
39. Weise, L. D., Nash, M. P. & Panfilov, A. V. A discrete model to study reaction–diffusion–mechanics systems. *PLoS ONE* **6**, e21934 (2011).
40. Quintanilla, J. G. *et al.*  $K_{ATP}$  channel opening accelerates and stabilizes rotors in a swine heart model of ventricular fibrillation. *Cardiovasc. Res.* **99**, 576–585 (2013).
41. Omichi, C., *et al.* Intracellular Ca dynamics in ventricular fibrillation. *Am. J. Physiol. Heart Circ. Physiol.* **286**, H1836–H1844 (2004).
42. Warren, M., Huizar, J. F., Shvedko, A. G., Zaitsev, A. V. Spatiotemporal relationship between intracellular  $Ca^{2+}$  dynamics and wave fragmentation during ventricular fibrillation in isolated blood-perfused pig hearts. *Circ. Res.* **101**, e90–e101 (2007).
43. Weiss, J. N., Garfinkel, A., Karagueuzian, H. S., Chen, P. S. & Qu, Z. Early afterdepolarizations and cardiac arrhythmias. *Heart Rhythm* **7**, 1891–1899 (2010).
44. Wang, L., *et al.* Optical mapping of sarcoplasmic reticulum  $Ca^{2+}$  in the intact heart: ryanodine receptor refractoriness during alternans and fibrillation. *Circ. Res.* **122**, 1410–1421 (2014).



**Extended Data Figure 1 | Electromechanical vortex filament dynamics during cardiac fibrillation.** **a**, 3D volumetric ultrasound speckle image showing a contracting isolated pig heart during ventricular tachycardia (same heart as shown in Fig. 1a, b, lateral imaging depth 6 cm). Mechanical filament (red) measured within ventricular wall (white region of interest; see also Fig. 1) between left and right ventricle. **b**, Validation of ultrasound measurement of mechanical filaments on the epicardium using optical mapping (voltage) confirms co-localized electrical and mechanical phase

singularities corresponding to two counter-rotating spiral waves (see also Fig. 1a). **c**, Breakthrough of an U-shaped intramural mechanical filament (red) on the epicardial surface of a pig heart results in the formation of two transmural filaments during ventricular fibrillation and two phase singularities (green circles) with opposite charge (counter rotation spirals) on the surface (see also Fig. 2a). Optical mapping (voltage and strain rate) confirms filament dynamics observed with 4D ultrasound.

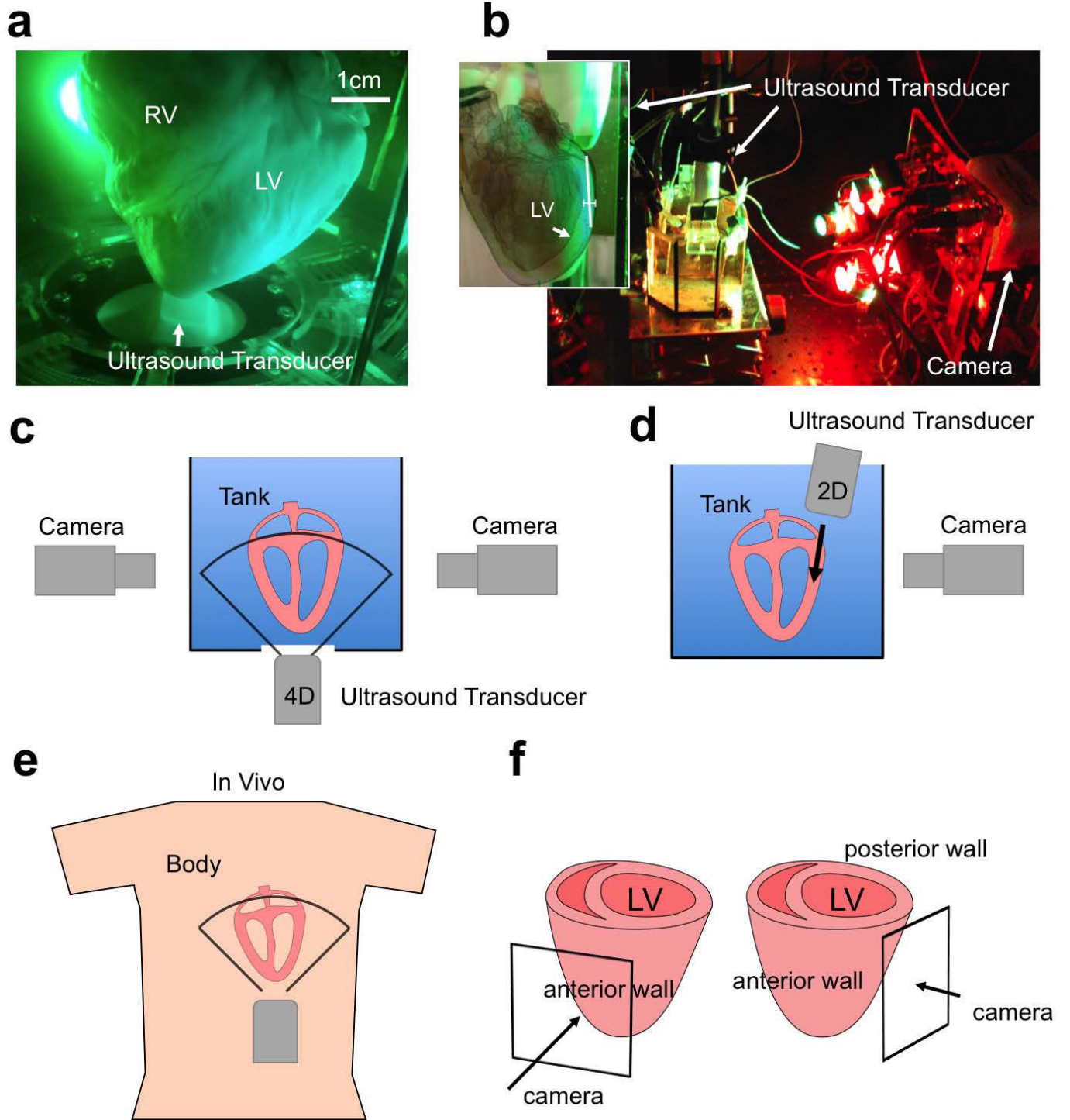


Extended Data Figure 2 | See next page for caption.

**Extended Data Figure 2 | 3D Imaging of electromechanical activity in the heart using simultaneous ultrasound and fluorescence imaging.**

**a–f**, Reconstruction of the heart shape during simultaneous imaging of electromechanical cardiac activity using ultrasound imaging and panoramic optical mapping. **a**, Photograph of heart in the Langendorff setup with ultrasound transducer at the bottom of the bath. LA, left atrium. **b**, 3D optical reconstruction of the surface of the heart obtained by rotating the heart after the experiment. Photorealistic rendering of the surface of the heart on reconstructed 3D surface mesh. **c**, Rendering (transparent) of 3D volumetric ultrasound speckle data showing the contracting heart from a similar perspective. Fan indicates lateral imaging depth of approximately 6–8 cm that was used for high-speed imaging. **d**, Optical mapping video images showing a bipolar electrode touching the epicardium of the left ventricle. The electrode is bend at the top, such that the tip is perpendicular to the electrode (only the tip touches the epicardium). The approximate location of the tip is indicated by the white rectangles in **a–d**, **g**, **i**. The 3D reconstruction allows the determination of the position of the electrode's tip on the heart surface from the two video images. **e**, Optical calibration target used for optical 3D reconstruction of

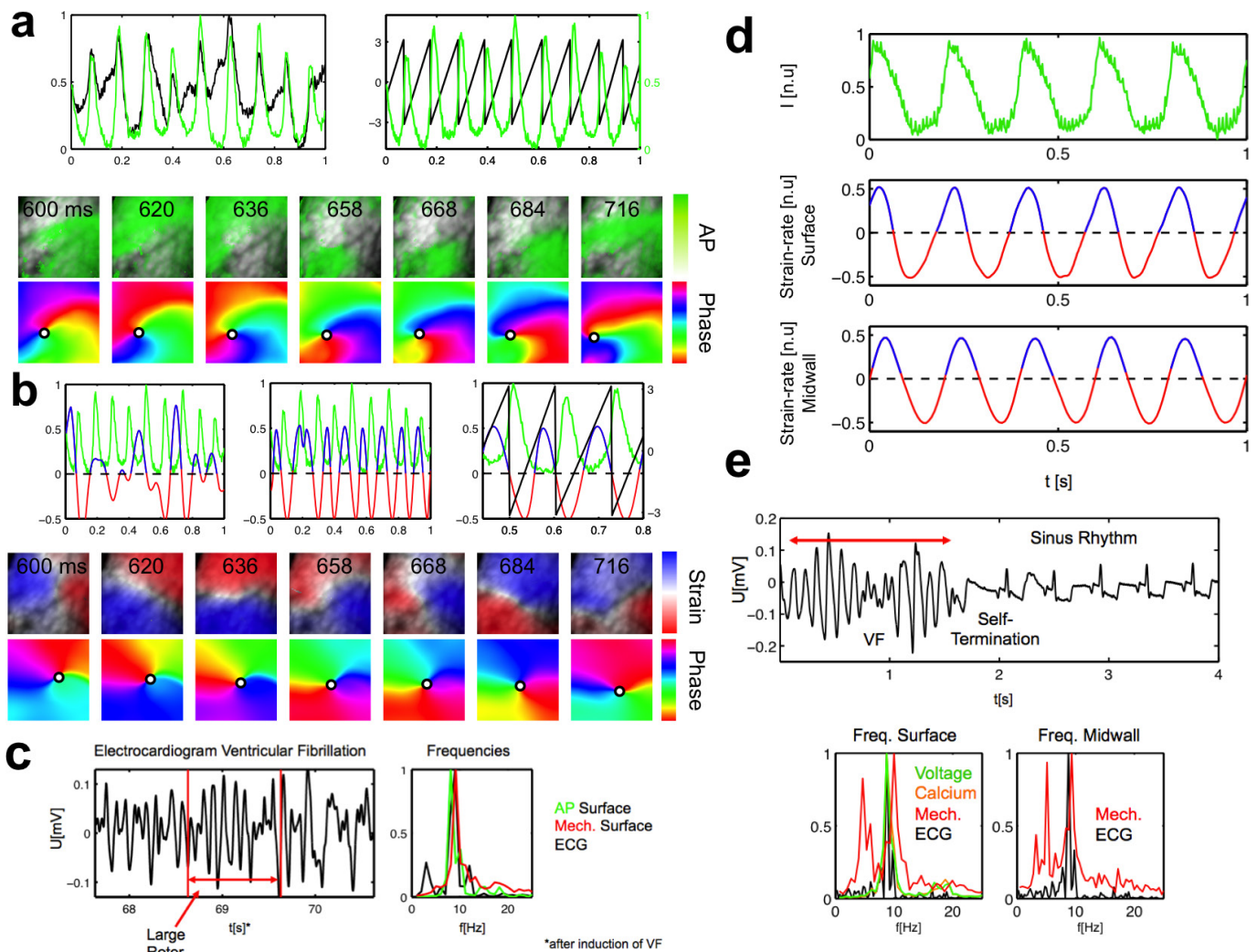
heart surface. **f**, Acoustic calibration target for ultrasound imaging used to determine approximate alignment and position of transducer. The inset shows the corresponding ultrasound speckle image of the calibration target at a particular depth. **g–j**, Focal electromechanical activity in a contracting pig heart mapped with optical mapping and ultrasound during pacing. **g**, Photorealistic rendering of optically reconstructed heart. The heart is rotated towards the left compared to **a**, **b**. **h**, Action potential wave propagating outwards (green arrows) from stimulation (voltage-sensitive mapping using Di-4-ANNEPS, black–white colour code: dark corresponds to depolarizing tissue or the upstroke of the action potential). **i**, 3D ultrasound speckle movie data showing same part of the heart (opaque and transparent rendering). **j**, Elastomechanical activation computed from 3D motion of the tissue acquired with ultrasound. The tissue starts to contract first at the stimulation site. The strain rate and its phase representation pattern exhibit a focal point that coincides with the stimulation site and the focal point that is visible in the optical maps. **a–d**, **g**, **i**, The region in which electrical pacing (stimulation) was applied to the heart is indicated with a rectangle.



Extended Data Figure 3 | See next page for caption.

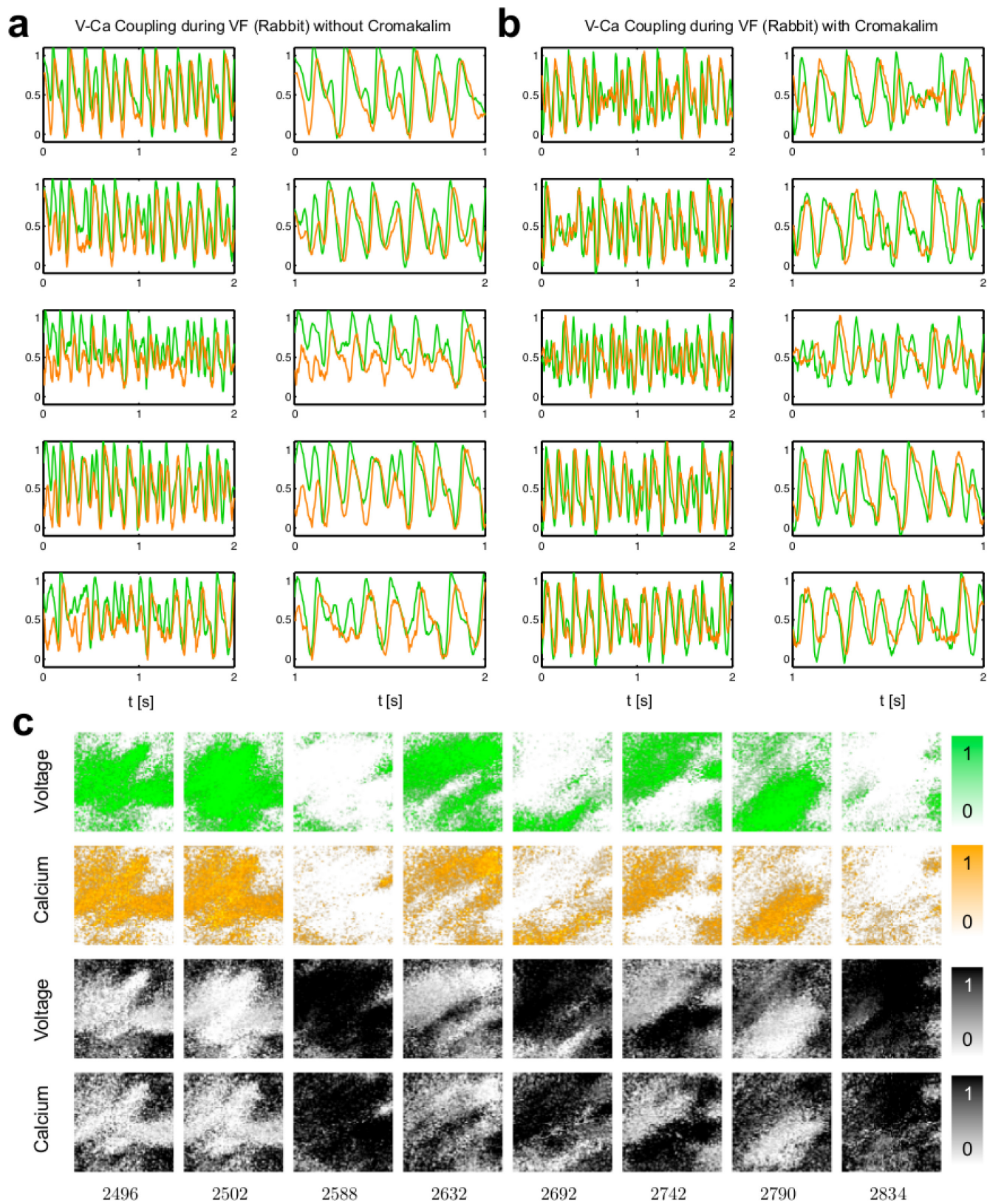
**Extended Data Figure 3 | Volumetric and cross-sectional ultrasound imaging and imaging configurations during *ex vivo* and *in vivo* imaging.** **a**, Isolated pig heart in imaging setup with 4D volumetric ultrasound transducer scanning from beneath the heart through an acoustic window, together with simultaneous panoramic fluorescence imaging (Fig. 1). 4D ultrasound imaging (Acuson sc2000, Siemens AG) was performed using a two-dimensional matrix phased-array transducer (4Z1c) producing volume frames with a pyramidal shape (51–188 volumes per second, maximum opening angle  $90 \times 90$  degrees, 6–14 cm lateral depth). The heart is aligned very similarly within the pyramid-shaped field of view as in an examination of a patient *in vivo*. **b**, Isolated rabbit heart in imaging setup with 2D cross-sectional ultrasound transducer scanning from above, together with simultaneous single-camera fluorescence imaging (see also **d** and Supplementary Video 9). **c**, Imaging configuration during 4D ultrasound imaging and panoramic multi-camera optical mapping with four cameras (see also **a**). The optical axis of the cameras and the lateral axis of the ultrasound scanner are approximately perpendicular. **d**, Imaging configuration during 2D ultrasound imaging and single-camera optical mapping (see also **b**). The optical axis of the camera and the lateral axis of the ultrasound scanner are approximately perpendicular. The cross-sectional ultrasound imaging plane is positioned

and aligned tangentially within the ventricular wall underneath and co-planar to the imaged surface. **e**, Imaging configuration during 3D ultrasound imaging *in vivo*. In ultrasound examinations of patients, the human heart is either imaged from outside the body through the chest in a transthoracic echocardiography (TTE) examination, or from within the body in a transoesophageal echocardiography examination using a transoesophageal ultrasound probe. The first measurement configuration provides a clearer picture of the ventricles, whereas the latter measurement provides a clearer picture of the atria. We aimed to mimic the TTE measurement imaging the ventricles using a probe that is routinely used in TTE examinations. In a TTE measurement, the transducer may be positioned on the chest below the heart imaging upwards through two ribs or from underneath the ribs. In one of the various views, the apex of the heart is facing the transducer (apical view), as it is located closest to the transducer array. The atria are located furthest away from the transducer array. The imaging configuration used in our experiment is very similar to this situation (**a**). The size of the human heart is comparable to the size of the pig hearts used in the *ex vivo* experiments. **f**, Frequent imaging configuration during 3D ultrasound imaging with panoramic optical mapping. One camera always imaged the anterior left ventricular wall (similar perspective as in **a**).



**Extended Data Figure 4 | Mapping and signal analysis of electromechanical rotor patterns during ventricular fibrillation and tachycardia in isolated Langendorff-perfused hearts.** **a**, Mapping of epicardial electrical (voltage) rotor activity during ventricular fibrillation on the contracting surface of a rabbit heart. Left, the time-series (black) obtained from the unstabilized fluorescence maps shows substantial motion artefacts, whereas the time-series of the motion-stabilized maps (green) shows a series of action potentials. Right, from the stabilized time-series, it is possible to compute the phase (black), that is, introducing phase jumps at the upstroke of the action potentials. Bottom, the upper image series shows a counter-clockwise-rotating action potential rotor (green) on the contracting heart surface (Supplementary Video 6). The lower image series shows the corresponding phase representation of the rotor and a phase singularity at the tip of the spiral. **b**, Left, time-series of strain rate obtained from the displacement field. Middle, normalized strain rate (see Methods). Right, zero-crossings of strain rate are used to obtain phase representation. Bottom, rotating wave of dilating (blue) and contracting (red) tissue regions rotating around each other and corresponding phase representation. A circle indicates the position of the mechanical phase singularity. Electrical and mechanical phase singularities are co-localized (Supplementary Video 6). **c**, Electrocardiogram during ventricular fibrillation (same heart as shown in **a**, **b**). Frequency spectra of electrocardiogram (black) and electrical

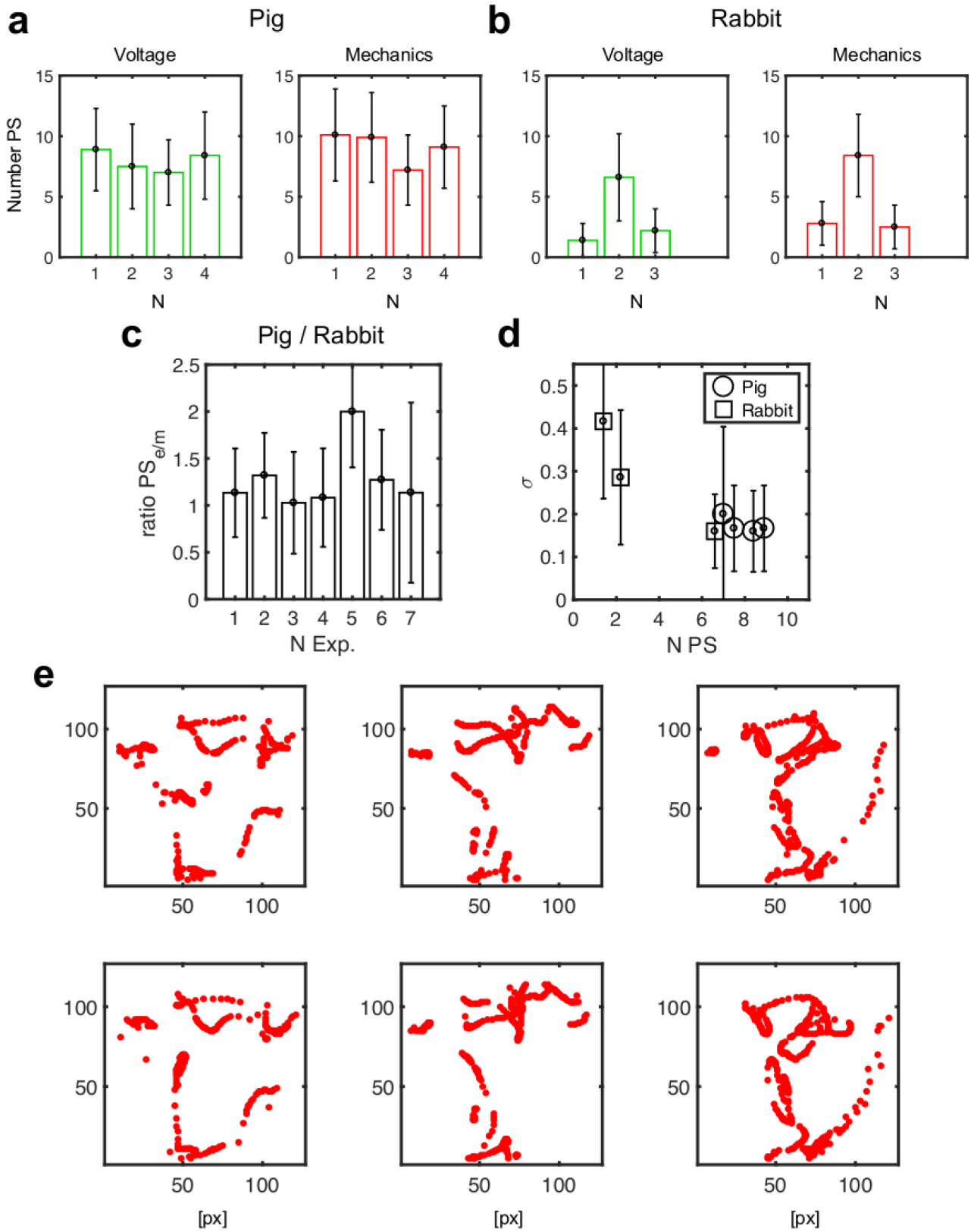
(voltage, green) and elastomechanical (red) patterns measured optically on the epicardial surface of the left ventricular wall (**a**, **b**), showing matching dominant frequencies ( $9 \pm 1$  Hz). Frequency spectra of the patterns are cumulative spectra of all measurement sites (Supplementary Video 6). **d**, Electromechanical activity in isolated pig heart during ventricular tachycardia (Fig. 1 and Extended Data Fig. 1b). Top, time-series of action potential activity measured optically using voltage-sensitive optical mapping on anterior left ventricular surface. Middle, time-series of strain rate measured optically in same location as in the top panel on left ventricular surface using fluorescence imaging. Bottom, time-series of strain rate measured within the anterior left ventricular wall using 4D ultrasound imaging. n.u., normalized units. **e**, Electrocardiogram acquired in the isolated rabbit heart during ventricular fibrillation (Fig. 4i). The arrhythmic episode ended by self-termination of arrhythmic activity and transition into sinus rhythm. Frequency spectra of electrocardiogram and electrical (voltage, green) and elastomechanical (red) patterns measured optically on the epicardial surface and elastomechanical (red) patterns measured using ultrasound at midwall inside the left ventricular wall during arrhythmic episode (including data within 2.0 s before self-termination). The dominant frequencies are  $9 \pm 1$  Hz for voltage, calcium and strain. Frequency spectra of the patterns are cumulative spectra of all measurement sites.



Extended Data Figure 5 | See next page for caption.

**Extended Data Figure 5 | Coupled voltage and calcium dynamics mapped during ventricular fibrillation.** Voltage (action potential, green, voltage-sensitive staining using Di4-ANBDQPQ) and calcium (intracellular calcium, orange, calcium-sensitive staining using Rhod2-AM) vortex wave activity mapped on ventricular surface of the isolated rabbit heart during ventricular fibrillation using dual-imaging<sup>29</sup>. Recordings were acquired in non-contracting hearts after administering of blebbistatin (4 ml diluted in 700 ml Tyrode, retrograde perfusion with constant reperfusion). **a, b**, Example time-series ( $n = 5$ ) of voltage–calcium activity chosen from arbitrary sites on the surface. Time-series show closely coupled voltage–calcium wave dynamics with a dominant frequency of  $9 \pm 1$  Hz and a delay of the calcium activity. **a**, Activity on the surface within 2 s long (left) and 1 s long intervals (right) to facilitate viewing of the upstrokes and the delay between voltage and calcium. Recordings acquired before administering (**a**) and after the addition of cromakalim (**b**, 10  $\mu$ mol in 1 l Tyrode, retrograde perfusion with constant reperfusion). We did not observe a noticeable difference in the dynamics. **c**, Voltage (action potential, green, voltage-sensitive staining using Di4-ANBDQPQ) and calcium (intracellular calcium, orange, calcium-sensitive

staining using Rhod2-AM) raw movies (black-and-white colour code) mapped on ventricular surface (field of view approximately  $1.5 \times 1.5$  cm<sup>2</sup>, time in ms) during ventricular fibrillation. The voltage-sensitive data are inverted (dimensionless normalized units (n.u.)), such that bright (or green) areas show depolarized tissue. Bright (or orange) areas in the calcium-sensitive data (dimensionless normalized units (n.u.)), show high intracellular calcium concentrations. The calcium-sensitive images show the same part of the tissue that is shown in the voltage-sensitive images, however, with a delay of 10 ms to compensate for the delay between voltage and calcium and to facilitate analysis of similar wave patterns. The patterns are highly similar and evolve congruently across the surface during ventricular fibrillation. Example image series chosen from a recording with a duration of 20 s. The findings are the same across different recordings. The experiment was repeated twice in  $n = 2$  hearts. However, other studies<sup>41–44</sup> have also shown that in abnormal voltage and calcium regimes the dynamics can have complex interactions and are not always necessarily closely coupled as shown here (see also Supplementary Discussion).



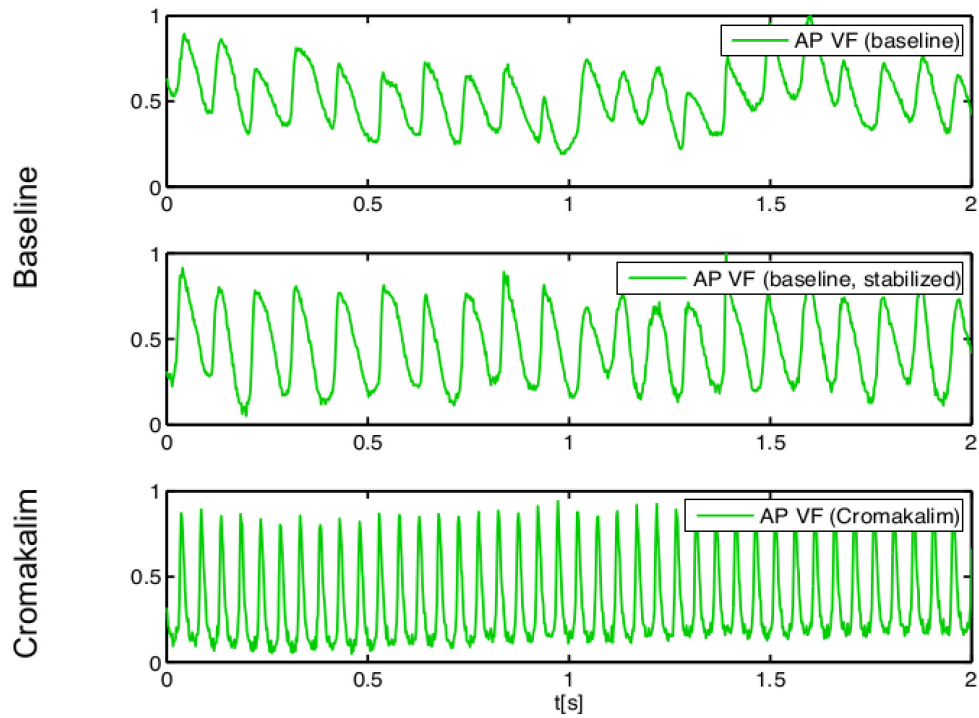
Extended Data Figure 6 | See next page for caption.

### Extended Data Figure 6 | Characteristics of epicardial electrical and mechanical phase singularities during ventricular fibrillation in pig and rabbit hearts.

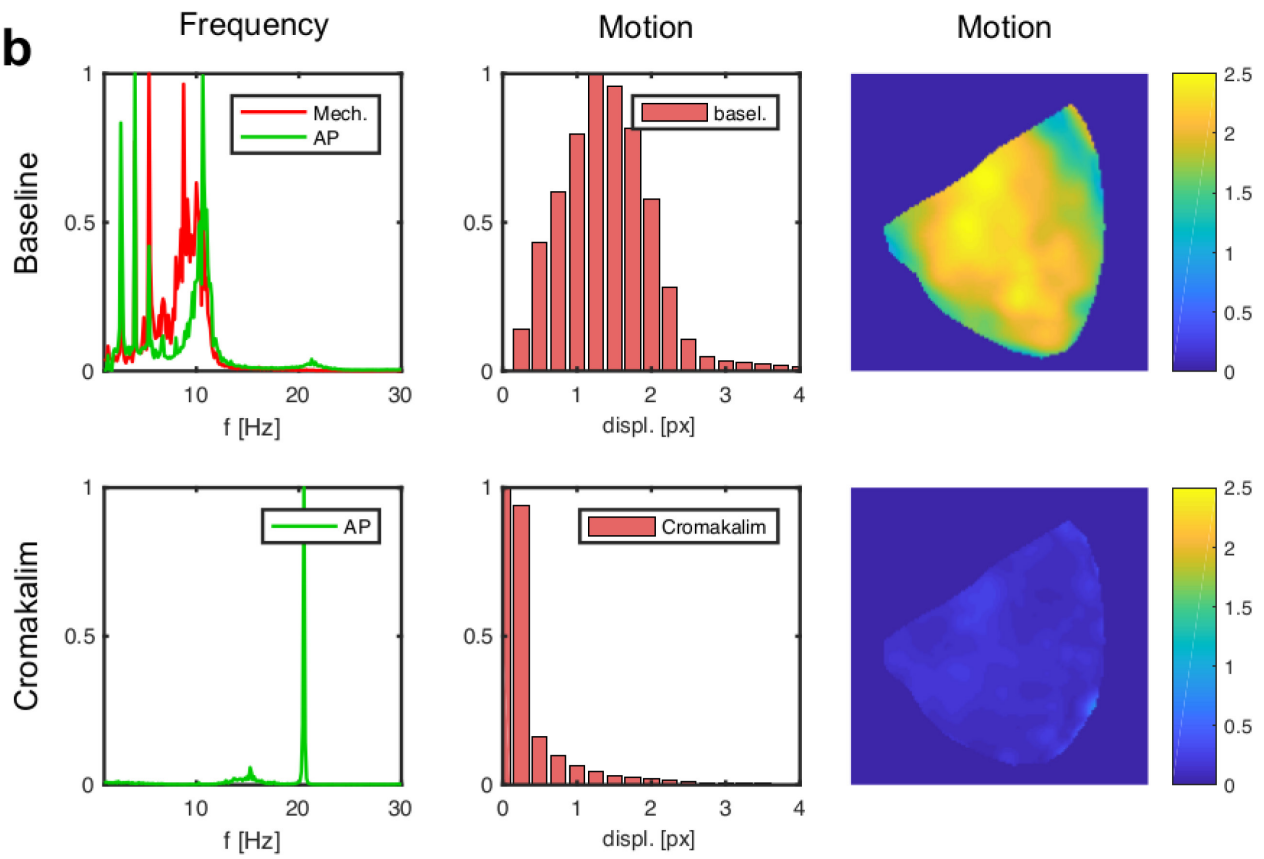
**a, b**, Mean number of electrical (green) and mechanical (red) phase singularities (PS) during ventricular fibrillation imaged on the epicardial ventricular surface of isolated Langendorff-perfused pig hearts (**a**; four measurements from  $n = 3$  hearts) and rabbit hearts (**b**; three measurements from  $n = 3$  hearts). The number of phase singularities fluctuates strongly over time (error bars indicate the standard deviation; see also Fig. 4g). Both the electrical and mechanical average numbers of phase singularities similarly reflect different regimes of ventricular fibrillation (**b**). We consistently observed a slightly larger number of mechanical phase singularities (factor  $1.2 \pm 0.1$ ). The average numbers of phase singularities were computed from 10-s long (500 frames per second) or 20-s long (250 frames per second) recordings with 5,000 video images, including  $>10,000$  measurements of phase singularities, the recordings were more than 100 times longer than the average period or lifetime of a rotor. **c**, Ratio of the mean number of electrical and mechanical phase singularities (ratio = number mechanical PS/number electrical PS) during ventricular fibrillation on epicardial ventricular surface of isolated Langendorff-perfused pig hearts (four measurements from  $n = 3$  hearts) and rabbit hearts (three measurements from  $n = 3$  hearts). The ratio is close to 1 ( $1.2 \pm 0.1$ ) and consistently larger than 1, indicating that more mechanical than electrical phase singularities appear on the surface during ventricular fibrillation. Error bars are large as the number of phase singularities fluctuates strongly (from 0 to approximately 10) over long times (Fig. 4g). Error bars were computed as the standard deviation of the fluctuations of number of phase singularities over time ( $>1,000$  samples or time-steps). The ratio (or centre of the plot) was computed from the simple average of the number of phase singularities ( $>1,000$  samples or time-steps). **d**, Co-localization factor sigma indicating the precision, with which a mechanical phase singularity describes on average the position of a nearby electrical phase singularity. For large phase singularity numbers ( $n_{PS} = 6-10$ ; right) the precision is about

0.2 or 1/5 of the average rotor distance (of 1). In this regime, two phase singularities can clearly be separated from each other (Fig. 4a). For the computation of sigma, the average rotor distances and co-localization distances from the distributions as shown in Fig. 3g and Fig. 4a were used. For smaller phase singularity numbers ( $n_{PS} = 1-3$ ; left) sigma increases, indicating that the precision with which a mechanical phase singularity predicts the location of an electrical phase singularity decreases. The two data points (on the left) describe dynamical regimes with few strongly meandering rotors with linear cores and larger overall deformations of the cardiac muscle (also data point 5 in **c**) during ventricular fibrillation in rabbit hearts (Fig. 3). However, lower sigmas were observed in both pig and rabbit hearts. Lower sigmas or a higher precision is obtained during ventricular fibrillation with a larger number of smaller rotors and a weaker overall deformation of the cardiac muscle. **e**, Trajectories of mechanical phase singularities during ventricular fibrillation on the surface of the rabbit heart. Mechanical phase singularities (red dots) computed individually from voltage-sensitive (top) and calcium-sensitive (bottom) imaging data during multimodal fluorescence imaging (voltage, calcium and strain) with interleaved acquisition of the two channels (250 frames per second per channel = 500 frames per second). The plots show the accumulated mechanical phase singularities during a 400-ms long time interval at 2 s (left), 4 s (centre) and 8 s (right) of a 20-s long recording. The positions and trajectories of the mechanical phase singularities computed from the voltage or the calcium data are identical or at least almost identical throughout time. The corresponding strain rate patterns, from which the phase singularities were computed, are also almost identical or highly similar in each frame over time. The positions and trajectories of the mechanical phase singularities and strain rate patterns are also identical or at least almost identical when only one dye is used and one of the channels does not contain a fluorescent signal. The data demonstrate that the optically derived strain rate patterns are robust, that is, independent of fluorescence-induced image intensity fluctuations.

**a**



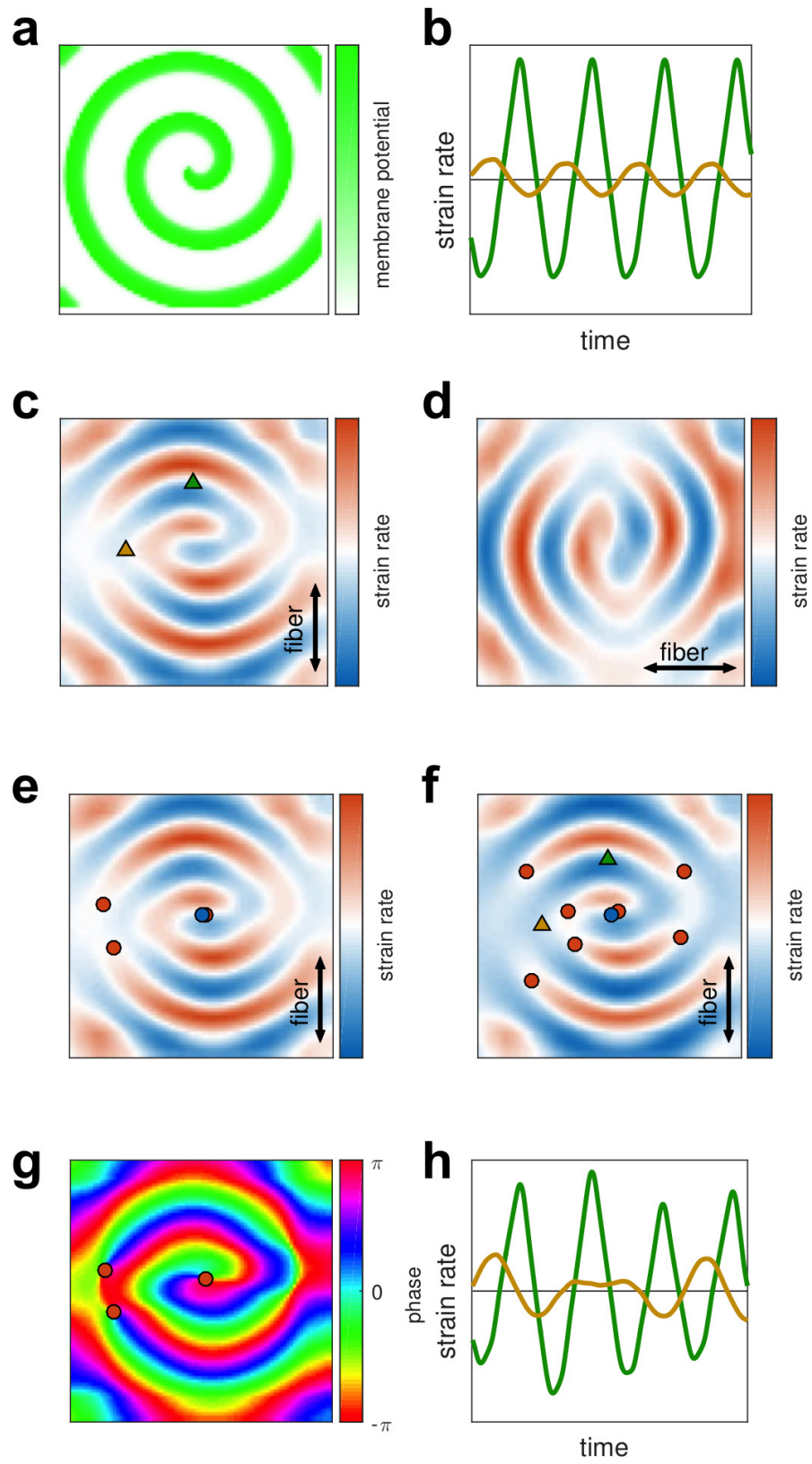
**b**



Extended Data Figure 7 | See next page for caption.

**Extended Data Figure 7 | Electromechanical dissociation and loss of contractility during very rapid (20 Hz) ventricular fibrillation in pig hearts. a.** Example traces of action potential wave activity measured on the left ventricular epicardial surface of a pig heart during ventricular fibrillation using multimodal optical mapping (voltage and contraction). Before the addition of the  $K_{ATP}$  channel opener cromakalim (baseline ventricular fibrillation, top), the ventricular muscle exhibits both fibrillatory electrical as well as contractile activity and associated deformations (see also Supplementary Video 12). Owing to the motion of the tissue, the optical traces are superimposed by motion artefacts, visible as modulations of the baseline of the signal. Motion stabilization and motion artefact removal retrieves the action potential wave activity (middle) with substantially reduced motion artefacts. The associated optical maps show spiral vortex wave patterns on the surface of the heart (see also Supplementary Video 12). The dominant frequency of the basal fibrillatory activity is  $10.6 \pm 1.5$  Hz (**b**). After the addition of cromakalim, the dominant frequency of the electrical activity increases markedly (compared to ref. 40) to  $20.5 \pm 0.5$  Hz, see **b**. At the same time, we measured that the heart does not exhibit any visible motion any longer (Supplementary Video 12). Because the contractions of the cardiac muscle vanish during very rapid ventricular fibrillation, optical maps and traces of the action potential wave activity can be retrieved without numerical motion tracking and motion stabilization (bottom). The modulations of the baseline of the signals, which can be seen during baseline ventricular

fibrillation (10 Hz), do not appear at very rapid ventricular fibrillation (20 Hz), indicating that motion is not present (Supplementary Video 12). The data demonstrate a decoupling of the electromechanical wave dynamics during very rapid ventricular fibrillation induced by cromakalim. **b.** Loss of contractile activity during very rapid (20 Hz) ventricular fibrillation. Frequency spectra of electrical action potential wave pattern (green) and mechanical activity (red) measured during baseline ventricular fibrillation (top left, maxima at approximately 10 Hz) and very rapid ventricular fibrillation (bottom left, 20 Hz peak). The dominant frequency of the action potential wave activity approximately doubles from 10 Hz to 20 Hz after the addition of cromakalim, as previously described<sup>40</sup>. At the same time, the contractile motion of the heart vanishes. Correspondingly, a frequency spectrum of the contractile or mechanical activity could not be computed during very rapid ventricular fibrillation. The histograms (middle) show large amplitudes of motion (1–3 pixels displacements of tissue segments within short time spans of 2–3 wave periods) during baseline ventricular fibrillation (top middle) and substantially reduced or vanishing amplitudes of motion (0–0.3 pixels displacements, Supplementary Video 12) during very rapid ventricular fibrillation (bottom middle). The amplitudes of motion were calculated from the displacement data obtained from the motion-tracking procedure. The corresponding maps (top right and bottom right) show the amplitudes of motion measured across the ventricular surface (yellow indicates 2–3 pixels displacement; blue indicates 0 pixels displacement).

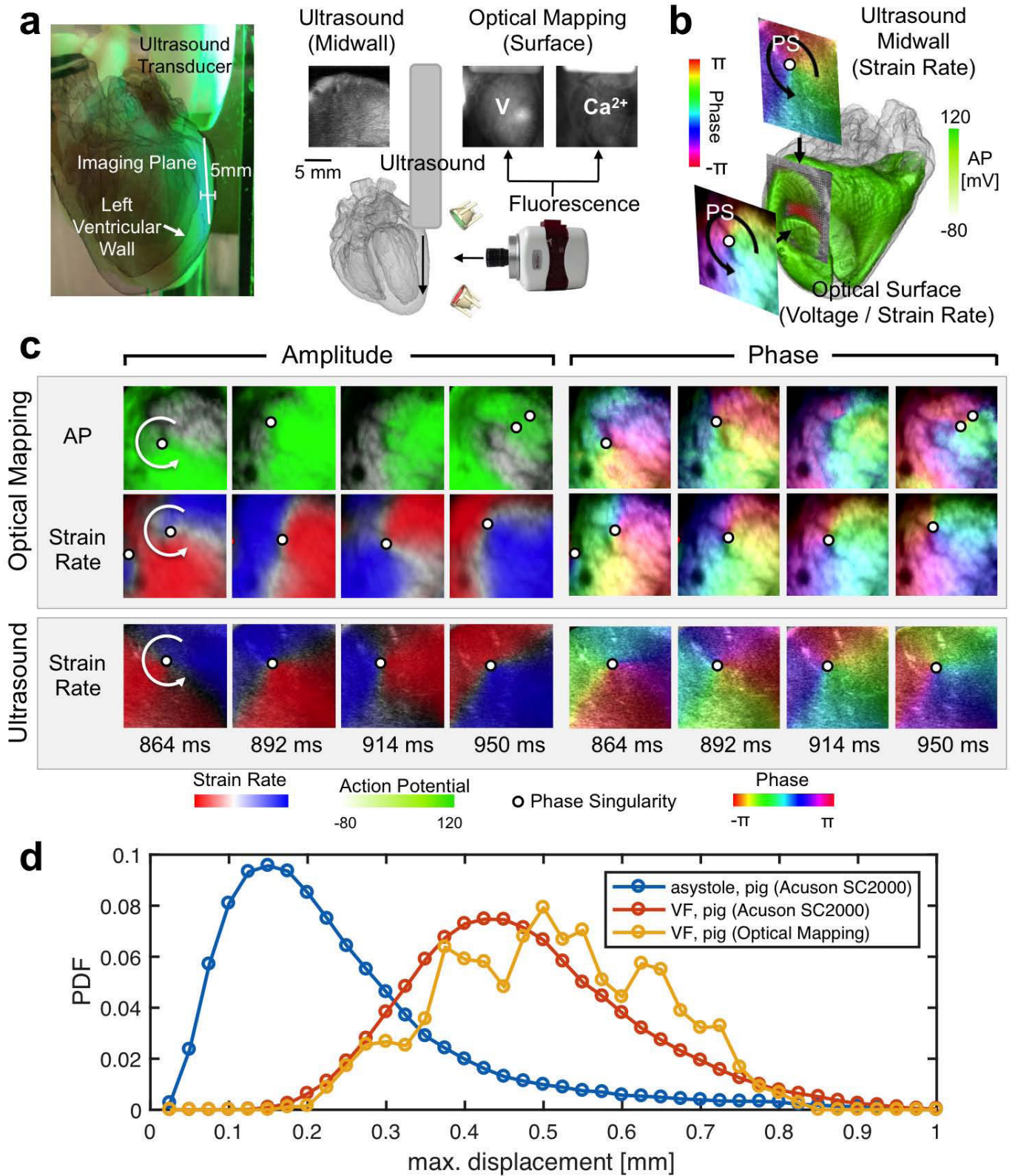


Extended Data Figure 8 | See next page for caption.

**Extended Data Figure 8 | Anisotropy of electromechanical rotor patterns in elastic excitable media (computer simulation) and effect of mechanical inhomogeneity onto mechanical phase singularities.**

**a, b, d.** Dependence of local strain rate amplitude and strain rate morphology on the direction of wave propagation relative to muscle fibres. The electrical spiral wave pattern (**a**) and corresponding elastomechanical strain rate patterns (**b, d**) form in two identically prepared simulation domains with differing underlying vertical (**b**) and horizontal (**d**) muscle fibre anisotropy (uniform transverse linear fibre orientation). **c.** The contractions along the fibre orientation produce stronger strain rate amplitudes when the wave propagates along the fibre orientation (green time-series in **b**, sampled from the green triangle) and weaker strain rate amplitudes when the wave propagates perpendicular to the fibre orientation (orange time-series in **b**, sampled from the orange triangle). Overall, the morphology of the strain rate pattern aligns with the fibre orientation and exhibits stronger gradients between dilating and contracting rates of deformation along the fibre orientation than perpendicular to it (polarization). The deformation data were obtained in quasi-2D electromechanical computer simulations with homogeneous active tension development and immediate electromechanical coupling and simulation domains with finite thickness (see Methods).

**e–h.** Sensitivity of phase singularity detection to external perturbations depending on the direction of wave propagation relative to fibres. **e.** Strain rate pattern superimposed with electrical (blue circle) and elastomechanical phase singularities (red circles) in a domain with uniform vertical fibre anisotropy. Perturbations caused by boundary conditions can distort the phase pattern and lead to the detection of spurious mechanical phase singularities, preferentially along the direction that is perpendicular to the fibre orientation. The spurious mechanical phase singularities propagate outwards away from the spiral wave core. **f.** Addition of a weak global strain perturbation exacerbates this effect in the direction that is perpendicular to the fibre orientation. **g.** Phase of strain rate shown in **e** used for the computation of the phase singularities also reveals anisotropy and polarization. **h.** The strong strain rate signal parallel to the fibre orientation (green time-series) is largely unaffected by a small perturbation, whereas, for the same perturbation amplitude, the strain rate signal in the low-amplitude region perpendicular to the fibre orientation is distorted more strongly (orange time-series). The deformation was obtained in simulations identical to those shown in **a–d**. Phase singularities from both the electrical signal and the strain rate were calculated using Hilbert transforms.



Extended Data Figure 9 | See next page for caption.

**Extended Data Figure 9 | Measurement of intramural phase singularity dynamics using 2D ultrasound imaging and tracking of a non-moving heart versus a fibrillating contracting heart in 3D ultrasound data and optical mapping.**

**a**, Schematic of the experimental setup for simultaneous fluorescence and 2D ultrasound imaging in intact, Langendorff-perfused rabbit hearts. Left, ultrasound imaging (Vevo 2100, VisualSonics Inc.) with the cross-sectional echocardiographic imaging plane aligned tangentially inside the left ventricular wall (white line). Imaging plane facing fluorescence imaging camera (Extended Data Fig. 3d). Right, action potential, calcium and strain imaging setup for fluorescence imaging.

**b**, Schematic of imaging configuration with action potential wave (phase) imaged on the surface of the heart and rotating mechanical pattern (phase) imaged inside the ultrasound cross-section inside the ventricular wall. The rendering shows a scroll wave (green, computer simulation).

**c**, Optical mapping shows a counter-clockwise rotating action potential wave (AP, green) on the surface of a rabbit heart during ventricular fibrillation (Supplementary Video 9). The electrical vortex is associated with a counter-clockwise rotating pattern of contractile (red) and tensile (blue) rates of strain observed optically with fluorescence imaging on the surface. The mechanical deformation observed in B-mode ultrasound imaging in an imaging plane located beneath the imaged surface and aligned approximately parallel or co-planar to the epicardium shows a phase singularity, corresponding to a counter-clockwise rotating wave in mechanical deformation (Supplementary Video 9). The analysis of the electrical and mechanical vortices reveals co-existing phase singularities (indicated by white circles) on the surface and inside the ventricular wall.

**d**, Tracking of the non-moving heart compared to a fibrillating contracting heart in 3D ultrasound and fluorescence imaging data. Distributions showing magnitudes of tracked displacement vectors resulting from motion tracking of the 3D ultrasound data (blue and red curves) and motion tracking during optical imaging (yellow curve). Influences by speckle noise or possible residual motion onto the motion tracking and motion analysis during ultrasound imaging are minimal in the Langendorff setup. Motion is not visible (Supplementary Video 13, left) when the heart does not contract. In comparison, the small contractions and deformations during ventricular fibrillation can clearly be observed (Supplementary Video 13, right) and can also be detected using motion-tracking algorithms (red curve, 3D ultrasound; yellow curve, optical mapping). The maximum of tracked displacements for the asystolic heart is approximately 0.15 mm. By contrast, during fibrillation, the maximum

displacements are clearly shifted towards larger values with a maximum at 0.45 mm. The magnitudes of the tracked displacements during ventricular fibrillation (red curve) are confirmed by the optical measurement performed at the same time (yellow curve). Statistical analysis (two-sample Kolmogorov–Smirnov test) rejects the null hypothesis that the ultrasound-based measurements of tissue displacement during asystole and ventricular fibrillation are from the same continuous distribution at a 1% significance level. For the ultrasound data, the distributions were obtained from 274,444 voxels (asystole) and 165,558 voxels (fibrillation), for which the displacements were tracked in between consecutive volume frames (with  $\Delta t = 1$  or  $\Delta t = 2$  or  $\Delta t = 3$ ) for the entire video sequence. Then only the maximal displacement in each voxel was stored and considered for the distributions to emphasize the influence of noise. Note in this context that in the asystolic case, tracking yields small displacement magnitudes due to measurement noise resulting presumably from both the algorithm and speckle noise. For a better comparison, the  $\Delta t$  or the temporal distance between volume frames between which motion was detected was adjusted. The asystolic data were imaged at volume rates of 62 volumes per second, whereas the fibrillation data was imaged at volume rates of 91 volumes per second. For the asystolic data (left), displacements were computed in between one and the second next volume frame ( $\Delta t = 2$ ), resulting in an effective volume rate of approximately 30 volumes per second. However, the distribution (left) remained unchanged with  $\Delta t = 1$ ,  $\Delta t = 2$  or  $\Delta t = 3$  frames, indicating that the tissue is static and does not exhibit motion. For the fibrillation data (right), displacements were computed in between one and the third next volume frame ( $\Delta t = 3$ ), resulting also in an effective volume rate of approximately 30 volumes per second. With  $\Delta t = 1$  or  $\Delta t = 2$  frames, the distribution also remains clearly distinguishable from the non-moving distribution and retains displacement magnitudes well over 0.5 voxels. Note that in this particular fibrillation dataset, the overall strength of motion and deformation is relatively small compared to other datasets (for instance the one shown in Fig. 1). In the optical data, displacements were computed from a frame at time  $t$  to a frame at time  $t + 32$  ms ( $\Delta t = 16$  frames) to achieve a corresponding measurement of tissue displacements at imaging speeds of approximately 30 frames per second and to ensure comparability of the data. The data and the clearly distinguishable visual appearance of the non-moving and fibrillating heart (Supplementary Video 13) demonstrate that the spatiotemporal resolution of the 3D ultrasound imaging is sufficient to resolve elastomechanical deformation patterns during tachyarrhythmias.

**Extended Data Table 1 | Statistics of electrical and mechanical phase singularity dynamics on the surface of fibrillating, contracting hearts ( $n=6$ )**

Exp.	# PS V	# PS M	Ratio M/V	Distance V-M [mm]	Dist. PS V [mm]	Dist. PS M [mm]	Ratio Distance V-M
<b>Pig</b>							
1	8.9 ± 3.4	10.1 ± 3.8	1.1	3.4 ± 1.7	20.6 ± 6.9	20.6 ± 6.9	0.17
2	7.5 ± 3.5	9.9 ± 3.7	1.3	3.4 ± 1.7	20.6 ± 6.9	20.6 ± 6.9	0.17
3	7.0 ± 2.7	7.2 ± 2.9	1.0	4.3 ± 4.3	21.5 ± 4.3	21.5 ± 4.3	0.20
4	8.4 ± 3.6	9.1 ± 3.4	1.1	3.4 ± 1.7	20.6 ± 6.9	20.6 ± 6.9	0.17
<b>Rabbit</b>							
5	1.4 ± 1.4	2.8 ± 1.8	2.0	2.9 ± 1.2	5.9 ± 1.2	7.0 ± 1.2	0.50
6	6.6 ± 3.6	8.4 ± 3.4	1.3	0.9 ± 0.5	5.3 ± 1.2	5.9 ± 1.2	0.17
7	2.2 ± 1.8	2.5 ± 1.8	1.1	2.3 ± 1.2	7.6 ± 1.9	8.2 ± 1.9	0.30

Measurements obtained by fluorescence imaging of the left ventricular surface of fibrillating, contracting pig ( $n=3$ ) and rabbit ( $n=3$ ) hearts. The fourth dataset (in the pig) was obtained in the same heart as the third heart, but in a different location (posterior instead of anterior left ventricular wall). Each data point corresponds to a recording, in which many hundreds of measurements were performed throughout the sequence of video images. The table shows similar numbers of electrical (V) and mechanical (M) phase singularities across hearts in the same species and similar ratios (M/V) across hearts and species, respectively. The measurements were obtained from several thousand video frames. In addition, the distances between electrical and mechanical (V-M) phase singularities are smaller than between equal (electrical–electrical or mechanical–mechanical) phase singularities across hearts and species, respectively. The data support the hypothesis that, on average, each electrical phase singularity can be associated with a nearby mechanical phase singularity. The average nearest neighbour distance between an electrical phase singularity and its corresponding mechanical phase singularity is small compared to or a fraction of the distance to the next electrical or mechanical phase singularity, respectively (in almost all cases the fraction is about 0.2).

## Life Sciences Reporting Summary

Nature Research wishes to improve the reproducibility of the work that we publish. This form is intended for publication with all accepted life science papers and provides structure for consistency and transparency in reporting. Every life science submission will use this form; some list items might not apply to an individual manuscript, but all fields must be completed for clarity.

For further information on the points included in this form, see [Reporting Life Sciences Research](#). For further information on Nature Research policies, including our [data availability policy](#), see [Authors & Referees](#) and the [Editorial Policy Checklist](#).

Please do not complete any field with "not applicable" or n/a. Refer to the help text for what text to use if an item is not relevant to your study. For final submission: please carefully check your responses for accuracy; you will not be able to make changes later.

### ▶ Experimental design

#### 1. Sample size

Describe how sample size was determined.

Proof-of-concept study with small sample size (N=6).

#### 2. Data exclusions

Describe any data exclusions.

No data was excluded.

#### 3. Replication

Describe the measures taken to verify the reproducibility of the experimental findings.

Findings were reproduced across species (pig, rabbit) and hearts (N=6 or 2 x N=3 for each species) and also confirmed in computer simulations.

#### 4. Randomization

Describe how samples/organisms/participants were allocated into experimental groups.

No randomization was used.

#### 5. Blinding

Describe whether the investigators were blinded to group allocation during data collection and/or analysis.

No blinding was done. Blinding was not relevant to our study as we were not able to assess or evaluate the data during the time of the data collection / measurement. Quantitative results were obtained or became obvious only after the completion of the data acquisition and after the analysis of the data.

Note: all in vivo studies must report how sample size was determined and whether blinding and randomization were used.

#### 6. Statistical parameters

For all figures and tables that use statistical methods, confirm that the following items are present in relevant figure legends (or in the Methods section if additional space is needed).

- | n/a                      | Confirmed  |
|--------------------------|--|
| <input type="checkbox"/> | <input checked="" type="checkbox"/> The <u>exact sample size</u> ( <i>n</i> ) for each experimental group/condition, given as a discrete number and unit of measurement (animals, litters, cultures, etc.)   |
| <input type="checkbox"/> | <input checked="" type="checkbox"/> A description of how samples were collected, noting whether measurements were taken from distinct samples or whether the same sample was measured repeatedly   |
| <input type="checkbox"/> | <input checked="" type="checkbox"/> A statement indicating how many times each experiment was replicated   |
| <input type="checkbox"/> | <input checked="" type="checkbox"/> The statistical test(s) used and whether they are one- or two-sided<br><i>Only common tests should be described solely by name; describe more complex techniques in the Methods section.</i>                       |
| <input type="checkbox"/> | <input checked="" type="checkbox"/> A description of any assumptions or corrections, such as an adjustment for multiple comparisons  |
| <input type="checkbox"/> | <input checked="" type="checkbox"/> Test values indicating whether an effect is present<br><i>Provide confidence intervals or give results of significance tests (e.g. P values) as exact values whenever appropriate and with effect sizes noted.</i> |
| <input type="checkbox"/> | <input checked="" type="checkbox"/> A clear description of statistics including <u>central tendency</u> (e.g. median, mean) and <u>variation</u> (e.g. standard deviation, interquartile range)  |
| <input type="checkbox"/> | <input checked="" type="checkbox"/> Clearly defined error bars in <u>all</u> relevant figure captions (with explicit mention of central tendency and variation)  |

See the web collection on [statistics for biologists](#) for further resources and guidance.

## ► Software

Policy information about [availability of computer code](#)

### 7. Software

Describe the software used to analyze the data in this study.

Commercial and custom software was used. The use of the commercial software (Matlab) is not critical and the same analysis can also be performed using freely available or custom software. The custom software (C++/OpenGL,VTK) can be used free of charge at any time and will be made available upon reasonable request. The code will be deposited in a community repository if requested.

For manuscripts utilizing custom algorithms or software that are central to the paper but not yet described in the published literature, software must be made available to editors and reviewers upon request. We strongly encourage code deposition in a community repository (e.g. GitHub). *Nature Methods* [guidance for providing algorithms and software for publication](#) provides further information on this topic.

## ► Materials and reagents

Policy information about [availability of materials](#)

### 8. Materials availability

Indicate whether there are restrictions on availability of unique materials or if these materials are only available for distribution by a third party.

There are no restrictions on availability of materials used in the study. All materials are commercially available (i.e. used chemicals).

### 9. Antibodies

Describe the antibodies used and how they were validated for use in the system under study (i.e. assay and species).

Not applicable.

### 10. Eukaryotic cell lines

a. State the source of each eukaryotic cell line used.

Not applicable.

b. Describe the method of cell line authentication used.

Not applicable.

c. Report whether the cell lines were tested for mycoplasma contamination.

Not applicable.

d. If any of the cell lines used are listed in the database of commonly misidentified cell lines maintained by [ICLAC](#), provide a scientific rationale for their use.

Not applicable.

## ► Animals and human research participants

Policy information about [studies involving animals](#); when reporting animal research, follow the [ARRIVE guidelines](#)

### 11. Description of research animals

Provide all relevant details on animals and/or animal-derived materials used in the study.

Goettingen Minipig (female, 21-26 months), New Zealand White Rabbit (female, 6-12 months).

All experiments were done in accordance with the German animal welfare law (§ 4 TierSchG) and were reported to our animal welfare representatives as well as the responsible authorities.

Policy information about [studies involving human research participants](#)

### 12. Description of human research participants

Describe the covariate-relevant population characteristics of the human research participants.

Not applicable.